JGR Atmospheres

RESEARCH ARTICLE
10.1029/2020JD034334

Evolution and Features of Dust Devil-Like Vortices in Turbulent Rayleigh-Bénard Convection—A Numerical Study Using Direct Numerical Simulation

S. Giersch[1] and **S. Raasch**[1]

[1]Institute of Meteorology and Climatology, Leibniz University Hannover, Hannover, Germany

Key Points:

- First direct numerical simulations of dust devil-like structures for Rayleigh numbers up to 10^{11} are presented
- Dust devils are strongly affected by Rayleigh number and surface friction but less affected by the aspect ratio of the model domain
- The 3-D structure of simulated dust devils is very similar to the one in large-eddy simulations of the atmospheric boundary layer

Correspondence to:
S. Giersch,
giersch@muk.uni-hannover.de

Citation:
Giersch, S., & Raasch, S. (2021). Evolution and features of dust devil-like vortices in turbulent Rayleigh-Bénard convection—A numerical study using direct numerical simulation. *Journal of Geophysical Research: Atmospheres*, *126*, e2020JD034334. https://doi.org/10.1029/2020JD034334

Received 30 NOV 2020
Accepted 8 MAR 2021

Author Contributions:
Conceptualization: S. Giersch, S. Raasch
Data curation: S. Giersch
Formal analysis: S. Giersch
Funding acquisition: S. Raasch
Investigation: S. Giersch
Methodology: S. Giersch, S. Raasch
Project Administration: S. Giersch, S. Raasch
Resources: S. Raasch
Software: S. Giersch, S. Raasch
Supervision: S. Raasch
Validation: S. Giersch
Visualization: S. Giersch
Writing – original draft: S. Giersch
Writing – review & editing: S. Giersch, S. Raasch

Abstract Dust devils are convective vortices with a vertical axis of rotation that are made visible by entrained soil particles. These soil particles contribute to the atmospheric aerosol input, influencing the Earth radiation budget. Quantifying this contribution requires reliable information about the statistics of dust devils, their formation process, and how they are maintained. In the past, this information was mainly derived from field experiments and large-eddy simulations (LESs). Field experiments suffer from the erratic occurrence of dust devils and the limited area that can be monitored reliably. In LESs, dust devils cannot be resolved completely, especially close to the ground. Additionally, they are affected by numerical features of surface boundary conditions, as well as subgrid-scale models in an unknown way. To mitigate these limitations, we employ direct numerical simulations (DNSs) to improve our understanding of dust devils. We comprehensively investigate the statistics and structure of dust devils for Rayleigh numbers up to 10^{11} using DNS of Rayleigh-Bénard convection between two plates for the first time. We find that dust devil-like structures occur in DNS with Rayleigh numbers much lower than in the atmosphere ($\geq 10^7$). These results support previous DNS studies in which vortices with vertical axes were observed but not further investigated. The dust devil statistics strongly depend on the Rayleigh number and velocity boundary conditions, but depend little on the aspect ratio of the model domain. Simulated dust devils show very similar properties to convective vortices analyzed in LESs of the atmospheric boundary layer.

1. Introduction

1.1. Motivation

Dust devils, also known as whirlwinds or willy willies, are organized, convective vortices with a vertically aligned axis of rotation. They occur on Earth (e.g., Bluestein et al., 2004; Sinclair, 1969) and Mars (e.g., Ellehoj et al., 2010; Kahanpää et al., 2016), and are made visible by soil particles (e.g., dust) that are swirled up from the ground. This makes dust devils not only a dynamically and optically interesting phenomenon (e.g., Kurgansky et al., 2016), but also a possible hazard to light aircraft (e.g., R. D. Lorenz & Myers, 2005) or future mars explorations (e.g., Balme & Greeley, 2006). In addition, they significantly increase the aerosol transport from the surface to the atmosphere on a regional (e.g., Gillette & Sinclair, 1990; Han et al., 2016; Ito et al., 2010; Renno et al., 2004) and global scale (e.g., Jemmett-Smith et al., 2015; Koch & Renno, 2005). Therefore, dust devils need to be considered in Earth's energy, carbon, and water cycle (Shao et al., 2011). However, quantitative estimates of the dust devils contribution to the overall amount of aerosols in the atmosphere are subject to great uncertainties (e.g., Han et al., 2016; Jemmett-Smith et al., 2015; Koch & Renno, 2005). To improve existing estimates, detailed statistical information on, i.e., the frequency of occurrence, strength, and dust fluxes of convective vortices is required. This demand has led to extensive research on dust devil-like structures through laboratory experiments (e.g., Greeley et al., 2003; Neakrase & Greeley, 2010), measurement campaigns (e.g., Murphy et al., 2016; Renno et al., 2004), and numerical investigations using large-eddy simulation (LES; e.g., Giersch et al., 2019; Kanak, 2005). Laboratory experiments have the disadvantage of being conducted in an artificial environment. This constraint limits the realism of the experiments. Alternatively, measurement campaigns are limited by the sporadic nature of dust devils that can be captured only in confined monitoring areas. Numerical simulations of dust devils have been performed over the past 20 years mainly due to a large increase in computing power (Spiga et al., 2016). However, numerical simulations via LES, from which the derivation of statistics would be straightforward,

are still unable to completely resolve the near-surface region, that is, the region most critical to the dust devil induced fluxes of heat and aerosols. Our study aims to extend the knowledge of dust devils by evading the previously mentioned disadvantages of experiments, measurements, and LES using direct numerical simulation (DNS) of Rayleigh-Bénard convection (RBC), an approach that has never been used before for a comprehensive study on dust devil-like structures.

So far, most numerical investigations of dust devils have been carried out employing LES, allowing simulations of convective vortices in the atmospheric boundary layer with a resolution down to a few meters (e.g., Giersch et al., 2019; Kanak, 2005; Ohno & Takemi, 2010; Raasch & Franke, 2011). However, LES requires the parameterization of unresolved sub-grid scale (SGS) processes. These are realized by SGS models that try to describe the influence of any turbulent process in the range of, or smaller than, the grid spacing on the resolved flow. The SGS models, as an inherent part of LES models, introduce errors, especially in those areas where small-scale mixing plays a crucial role (e.g., Sorbjan, 1996; Sullivan et al., 1994). The surface layer is a typical example of such an area (Spiga et al., 2016). Dust-devil like structures are located in the surface layer and might be influenced by the SGS model that is used. Although Kanak (2005) does not believe that the choice of the SGS closure scheme would make a difference between the existence or nonexistence of vertical vortices in LES simulations, an influence on dust devil quantities cannot be excluded. In addition to the parameterization of turbulent diffusion through the SGS model, the surface layer requires careful and realistic treatment of model surface stresses and surface heat fluxes. Typically, this is realized by using bulk parameterizations (e.g., Kanak, 2005; Ohno & Takemi, 2010) or Monin-Obukhov similarity theory, which implies the assumption of a constant flux layer between the surface and the first grid level (e.g., Giersch et al., 2019; Raasch & Franke, 2011). A quantification of the uncertainties of dust devil statistics caused by parameterizations is still missing. LES grid convergence studies down to grid spacing of less than 1 m would overcome this shortcoming, but a too high demand on computational resources has been prohibited such studies so far. In DNS, however, neither the parameterization of SGS processes nor the parameterization of surface stresses and heat fluxes are required. Therefore, no parameterization uncertainties must be considered. This study will compare DNS results of dust devil-like vortices with LES results, to illuminate potential effects of parameterizations used in LES on the dust devil structure.

Although DNS is an appropriate tool for studying dust devil-like vortices, only a few publications exist that show first steps toward a comprehensive investigation of their structure and statistics. Cortese and Balachandar (1993) recognized strong vertical vorticity in thermal plumes, resulting in spiraling hot updrafts and cold downdrafts. Fiedler and Kanak (2001) investigated intense columnar vortices in RBC. They discovered similarities between dust devils investigated with DNS and LES. However, both studies lack statistics and quantitative features of dust devils in DNS simulations. In addition, Cortese and Balachandar (1993) and Fiedler and Kanak (2001) only considered free-slip boundary conditions for Rayleigh numbers up to 10^7. Therefore, their investigations did not allow for frictionally induced flow convergence toward the vortex center. Iijima and Tamura (2008) investigated the formation process and the physical mechanism of strong vertical vortices in convection with and without applying external forces. These forces caused artificial, anticlockwise rotation in the flow field and an upward flow component with the aim to strengthen the naturally developing vertical vortices in their simulations by vorticity concentration and vortex stretching. Still, also Iijima and Tamura (2008) did not provide any detailed statistical, structural, or quantitative features of vertical vortices that develop in natural convection. Consequently, our DNS study aims to allow a free, frictionally influenced development of vortices, by convection alone, for Rayleigh numbers up to 10^{11} to mimic the planetary boundary layer as much as possible.

Even if no-slip boundary conditions better represent a realistic environment under which dust devils develop, a simulation with free-slip conditions will also be carried out to analyze and quantify the effect of surface friction on dust devil statistics. The strong and nontrivial effects of surface friction on vertical vortices has been already investigated in other studies. For example, Gu et al. (2010) simulated dust devils with the help of initial tangential velocity and found that surface friction significantly affects the near-surface shape of dust devils. The laboratory-like simulations from Neakrase and Greeley (2010), focusing on the sediment transport of dust devils, showed that vortex size increases and tangential velocity decreases as surface roughness is increased. In addition, they found that a small increase in surface roughness enables reduced threshold velocities to lift fine particles from the surface. Also, LES studies of the atmospheric,

convective boundary layer show significant effects of near-surface, frictionally induced horizontal vorticity on dust devil development (e.g., Giersch et al., 2019; Kanak et al., 2000; Raasch & Franke, 2011). Ito and Niino (2013) claim that effects of surface friction are not essential for the formation of dust devil-like vortices and that absolute values of vertical vorticity and the overall convection pattern are similar between simulations with and without surface friction. Thus, the consequences of applying free-slip boundary conditions on dust devil statistics will be clarified in this study.

Flow properties and structures in RBC are strongly influenced by the Rayleigh number $Ra = \alpha g \Delta\theta H^3/(\nu\kappa)$, as well as the aspect ratio $\Gamma = L/H$ (e.g., Bailon-Cuba et al., 2010; Pandey et al., 2018; Stevens et al., 2018). Here, α is the thermal expansion coefficient, g the gravitational acceleration, $\Delta\theta$ the potential temperature difference between the lower and upper plate, H the distance between the plates, ν the kinematic viscosity, κ the thermal diffusivity, and L the lateral extent of the model domain. Bailon-Cuba et al. (2010) found that large-scale patterns in time-averaged flow fields change from a one-roll to a two-roll flow pattern at around $\Gamma = 2.5$ for Rayleigh numbers 10^7 and 10^8. However, they have also shown that the exact aspect ratio needed for getting a multi-roll system depends on the Rayleigh number and that there is a reorganization of flow from the roll shape to pentagonal or hexagonal structures with increasing Γ (up to 12) for a fixed Ra. This is true for a fixed Γ with increasing Ra (up to 10^8), as well. Consistent with these structural changes in flow patterns, flow statistics in RBC are strongly modified by the Rayleigh number and aspect ratio. Stevens et al. (2018) concluded from their investigations of thermal superstructures that integral quantities such as the Nusselt number converge for $\Gamma = 4$. Reaching a convergence of the peak location of the temperature variance and turbulent kinetic energy (TKE) spectra requires an astonishing aspect ratio of 64. The previously cited findings make it very likely that dust devil evolution depends on Rayleigh number and/or aspect ratio, because the existence of vertical vortices appears to be tied to specific flow patterns (Kanak, 2006). To study this, Ra and Γ will be varied between 10^6 and 10^{11} and 2 to 4, respectively.

This study will offer an overview of the effects of surface friction, Rayleigh number, and aspect ratio on dust devil statistics, providing the first comprehensive DNS investigation of dust devil-like structures. The study is organized as follows. The applied simulation setups and analysis methods are described in Section 2. The results are presented in Section 3. A summary and conclusions are given in Section 4. The appendix details validation results of the DNS mode of the numerical model used in this study. In addition, further information on resolution requirements and a grid resolution study are presented.

1.2. Dust Devil Formation and Maintenance

This subsection will briefly summarize the vortex formation and maintenance hypothesis established by Raasch and Franke (2011) because it will be frequently used in the following discussion. The budget equation for the vertical vorticity reads (see also Raasch & Franke 2011):

$$\frac{\partial \zeta}{\partial t} = -(\vec{v}_\mathrm{h} \cdot \vec{\nabla}_\mathrm{h})\zeta - w\frac{\partial \zeta}{\partial z} - \underbrace{\zeta(\vec{\nabla}_\mathrm{h} \cdot \vec{v}_\mathrm{h})}_{\zeta_\mathrm{div}} - \underbrace{\frac{\partial w}{\partial x}\frac{\partial v}{\partial z} + \frac{\partial w}{\partial y}\frac{\partial u}{\partial z}}_{\zeta_\mathrm{twi}} + \nu\nabla^2\zeta, \tag{1}$$

where $\vec{v}_\mathrm{h}$ represents the horizontal velocity vector and $\vec{\nabla}_\mathrm{h}$ is the nabla operator in the horizontal direction. The Coriolis and solenoidal terms have been neglected here. The Coriolis force is not considered in the simulated DNS setups at all and the solenoidal term, which describes the generation of vertical vorticity by baroclinic processes, does not exist under the Boussinesq-Approximation used in this study (see Section 2). Equation 1 indicates that vertical vorticity can be modified by the so-called twisting term, ζ_twi, which describes the transformation of horizontal vorticity into the vertical direction. It is the only term in the above equation that can generate vertical vorticity from a flow that did not previously rotate around the vertical axes. The remaining terms are only able to rearrange existing vertical vorticity by advection, increasing/decreasing it by convergence/divergence of the horizontal velocity field, ζ_div, or equalizing it by molecular diffusion. A detailed analysis of the budget equation by Raasch and Franke (2011) indicates that the rotation of a dust devil is maintained by a combination of convergence and twisting effects. The convergence

effect is caused by the strong updraft that is located above a dust devil. The updraft provokes near-surface flow convergence, which further concentrates vorticity in the vortex core. This process is represented in the vorticity budget equation by ζ_{div}. Additionally, horizontal vorticity created by the vertical shear near the surface is converted to vertical vorticity as soon as the flow enters the updraft region around the vortex core. This is described in Equation 1 by ζ_{twi}. Some values for the twisting, divergence and advection terms are stated in Section 3.5.

The budget equation for the vertical vorticity from above can be used to describe how the vortex maintains its vertical vorticity. But because the equation already assumes an initially rotating flow, it does not explain where and why vortices form at all (see also, Raasch & Franke, 2011; S. Rafkin et al., 2016). It is already known that dust devils occur mainly at the vertices of the hexagonal cells that develop in the convective boundary layer (e.g., Giersch et al., 2019; Kanak, 2005; Raasch & Franke, 2011). Raasch and Franke (2011) argue that the initial vertical vorticity at these vertices is created by chance in the following way: the flow converges at the cell vertices due to high vertical wind velocities occurring there. Normally, this happens in a nonuniform way with velocity components of different strength pointing toward the convergence lines, which are located around the vertex and are merging in its center. By chance, the flow might have a structure where the overall vertical vorticity of the flow around the vertex is nonzero (see Figure 15a in Raasch & Franke, 2011). This initial vorticity is then further concentrated by the general flow convergence and a vortex is created.

2. Methodology

In the following, a dust devil is defined as a convective vortex exceeding certain core pressure drop and vertical vorticity thresholds (see Section 2.2). Furthermore, (convective) vortex, dust devil, and dust devil-like vortex are used as synonyms.

All numerical simulations are carried out with the PALM model system (Maronga et al., 2020), which has been specifically designed for LES studies of the atmospheric boundary layer (e.g., El Guernaoui et al., 2019; Heinze et al., 2012; Maronga & Raasch, 2013). In this study, however, PALM will be used in DNS mode, in which every turbulent fluctuation is resolved. This is possible by using PALM's default system of equations as mentioned in Maronga et al. (2015) and assuming constant diffusivities equal to the molecular values of the fluid. The nonhydrostatic and nonfiltered incompressible system of equations in Boussinesq-approximated form are then:

$$\frac{\partial u_i}{\partial t} = -\frac{\partial u_i u_j}{\partial x_j} - \frac{1}{\rho_0}\frac{\partial p^*}{\partial x_i} + g\frac{\theta - \langle\theta\rangle}{\langle\theta\rangle}\delta_{i3} + \nu\frac{\partial^2 u_i}{\partial x_j^2}, \tag{2}$$

$$\frac{\partial u_j}{\partial x_j} = 0, \tag{3}$$

$$\frac{\partial \theta}{\partial t} = -\frac{\partial u_j \theta}{\partial x_j} + \kappa\frac{\partial^2 \theta}{\partial x_j^2}. \tag{4}$$

Equations 2–4 describe the conservation of momentum, mass, and thermal internal energy, respectively. Here, $i, j \in \{1, 2, 3\}$. u_i are the velocity components along x, y, and z. t is the time, and ρ is the density of dry air. p^* represents the perturbation pressure, $g = 9.81$ m s^{-2} is the gravitational acceleration, and δ is the Kronecker delta. Finally, $\langle\cdot\rangle$ indicates a horizontally averaged value at a fixed height and a subscript zero denotes a surface value. No Coriolis or large-scale pressure gradient forces are considered here. Neither of these forces affect the fluid in classical RBC.

Time integration of the above set of equations is realized by using a third-order Runge-Kutta scheme (Williamson, 1980). The advection terms are approximated by a fifth-order scheme from Wicker and

Skamarock (2002), which well conserves strong gradients that frequently occur in dust devils, covering only a couple of grid points (e.g., Giersch et al., 2019). To guarantee the incompressibility condition (3), a predictor-corrector method is used (e.g., Patrinos & Kistler, 1977), in which a Poisson equation for p^* is solved after every time step. As done in similar studies of dust devils with horizontally homogeneous setups, the absolute value of p^* is interpreted as the pressure drop within dust devils (e.g., Giersch et al., 2019; Kanak, 2005; Raasch & Franke, 2011). Here, PALM's DNS mode is used for the first time. Therefore, a validation of the DNS mode was carried out. A short summary of the validation is provided in Appendix A.

2.1. Numerical Setups

This subsection will give an overview of the simulations that have been conducted to study dust devil-like structures in RBC between two flat plates. The selected simulation parameters shall enable a comparison with laboratory experiments (e.g., du Puits et al., 2007). In all cases, air is considered at 1013.25 hPa with a domain-averaged temperature of $\theta_{ref} = 303.15$ K. With these pressure and temperature values, the constant fluid properties ν and α are set to 1.598×10^{-5} m^2 s^{-1} and 3.32×10^{-3} K^{-1}, respectively. α is only specified here to allow the recalculation of the Rayleigh number. For solving the model equations, the exact value of the thermal expansion coefficient is irrelevant. A Prandtl number $Pr = \nu/\kappa = 0.7$ is assumed.

At the impermeable plates, no-slip boundary conditions ($u = v = 0$) are applied in most of the cases. Only once, free-slip conditions ($\partial u/\partial z|_{wall} = \partial v/\partial z|_{wall} = 0$) are assumed to study the effects of friction on the vortices. Additionally, a Neumann condition for the perturbation pressure is set at the bottom and top boundary ($\partial p^*/\partial z|_{wall} = 0$). The forcing of convection is realized by applying a fixed temperature difference $\Delta\theta = \theta_1 - \theta_2$ of 40 K between the lower ($\theta_1 = 323.15$ K) and upper plate ($\theta_2 = 283.15$ K). These temperature values allow a direct comparison with experimental results, for example, derived from the Barrel of Ilmenau (e.g., du Puits et al., 2007, 2013). Such a comparison is already planned for the near future (see also Section 4). The temperature difference of 40 K might question the application of the Boussinesq-approximation. However, according to Bazdidi-Tehrani et al. (2018), Gray and Giorgini (1976), and Niemela and Sreenivasan (2003) the approximation is applicable here and uncertainties due to nonBoussinesq effects are limited to several percent. In the horizontal directions, cyclic boundary conditions are used.

The domain size is quadratic horizontally and characterized by the variable height ($0.066\text{ m} \le H \le 3.036$ m) or Rayleigh number ($10^6 \le Ra \le 10^{11}$) and the aspect ratio ($2 \le \Gamma \le 4$). Because dust devil-like structures have been found to be connected to the cellular pattern that develops within the convective, atmospheric boundary layer (e.g., Giersch et al., 2019; Kanak, 2006; Kanak et al., 2000; Raasch & Franke, 2011), a sufficiently large aspect ratio is required to allow for the development of these hexagonal cells. In LESs of the atmospheric boundary layer, a ratio of three between the horizontal model extent and the height of the mixed layer is sufficient (e.g., Kanak et al., 2000). However, DNS of RBC shows that stationary hexagonal cell structures would require aspect ratios of 12 or more (e.g., Bailon-Cuba et al., 2010; von Hardenberg et al., 2008), which is not feasible with the Rayleigh numbers under study and present-day computing power. As a compromise between domain size and computing costs, a ratio of three is selected for most of the simulations. Consequently, the hexagonal cells that appear are nonstationary. They grow in time before they finally approach the domain size (see Section 3). Nevertheless, an aspect ratio of three allows for the calculation of sufficient dust devil statistics. For Rayleigh numbers of up to 10^8, DNSs with 1 mm grid spacing are carried out. In case of higher Rayleigh numbers, the grid spacing is uniformly set to 2 mm, as a compromise between resolution and computing costs. Two millimeter grid spacing is still fine enough to adequately simulate the bulk of the flow (see Appendix B for a grid resolution study). The simulated time is restricted to 100 s. This is another compromise between computational costs and providing sufficient statistics of dust devils, which heavily depend on domain size and simulated time.

At initialization, zero velocities are assumed everywhere and their mean values remain zero for all times. The initial condition for the potential temperature at every x, y position is defined as in Mellado (2012) through

$$\theta(z) = \begin{cases} \theta_{\mathrm{ref}} + (\theta_1 - \theta_{\mathrm{ref}})\left[1 - \mathrm{erf}\left(\dfrac{\sqrt{\pi}\, z}{2\delta_{\mathrm{t}}}\right)\right] & \text{for } \dfrac{z}{H} \le 0.5, \\ \theta_{\mathrm{ref}} + (\theta_2 - \theta_{\mathrm{ref}})\left[1 - \mathrm{erf}\left(\dfrac{\sqrt{\pi}\,(H - z)}{2\delta_{\mathrm{t}}}\right)\right] & \text{for } \dfrac{z}{H} > 0.5, \end{cases} \tag{5}$$

where $\delta_{\mathrm{t}} = 11\Delta z$ is the thickness of the initial temperature profile with Δz being the vertical grid spacing (see Figure 2 for initial potential temperature profile). In addition to the unstably stratified fluid, random perturbations are necessary to trigger the onset of convection. These perturbations are imposed on the horizontal velocity field at the beginning of the simulation.

Table 1 summarizes all conducted simulations together with the varied parameters: domain size, number of grid points, grid spacing, velocity boundary condition, Rayleigh number, and aspect ratio. Each simulation is accompanied by an identifier (ID), which will be used as a reference henceforth. Each ID consists of the Rayleigh number ("RA") and the aspect ratio ("A"). The simulation with free-slip boundary conditions at the plates is marked with an asterisk.

2.2. Vortex Detection and Analysis

The vortex detection and analysis algorithm explained in Raasch and Franke (2011) and Giersch et al. (2019) is used for determining the averaged features of dust devil-like vortices. This subsection will mention the points of the algorithm that are relevant for the discussions in this study. Also changes and additions to Raasch and Franke (2011) and Giersch et al. (2019) will be noted.

The vortex center detection is realized during a run after each model time step by identifying local minima of the perturbation pressure drop and local maxima of the absolute value of the vertical vorticity, which corresponds to the vertical component of rotation of the velocity field

$$|\,\zeta\,| = \left|\,\frac{\partial v}{\partial x} - \frac{\partial u}{\partial y}\,\right|. \tag{6}$$

Here, the derivatives are approximated by difference quotients over one grid spacing. These difference quotients are subsequently interpolated onto the scalar grid point. PALM uses a staggered grid. Therefore, the horizontal velocity components are defined at the grid volume edges, whereas all scalars are defined at the center. Furthermore, the horizontal velocity components and scalars are vertically shifted by half the grid spacing compared to the vertical component and the first grid point above the surface is defined at $\Delta z/2$. The detection procedure is only executed at the first grid plane above the bottom surface, that is, at 0.5 mm for RA1006A3, RA1007A3, RA1008A3 and at 1 mm for all other simulations in Table 1. Due to the symmetry of the studied setups, vertical vortices also occur at the upper plate, which are neglected for technical reasons (The detection and analysis algorithm was originally designed for atmospheric vortices that are bounded at the lower surface). Even if they would be considered, it is not expected that they would improve the vortex statistics because structures at the bottom and top plate are strongly correlated.

In order to consider a local pressure minimum and vorticity maximum as a dust devil-like vortex, thresholds must be defined. Whenever the defined thresholds are exceeded, the information related to the vortex (e.g., the position) is recorded. As explained in Giersch et al. (2019), 5 times the standard deviation of vorticity and 3 times the standard deviation of perturbation pressure are defined as the thresholds. The standard deviation is calculated as a mean value derived from 8 instantaneous horizontal cross sections taken from the analysis height between 30 and 100 s simulated time (every 10 s). For each cross section, a single standard deviation is calculated. Subsequently, an arithmetic mean is determined and used to compute the thresholds. The first 30 s of the simulations are not taken into account for dust devil detection and analysis because of the model spin-up phase (see Section 3.1). Because standard deviations vary strongly with Rayleigh number, simulations with different Rayleigh number causes different detection thresholds. Table 2 displays the threshold values used for each simulation. For example, a dust devil-like vortex is identified only if $|p^*|$ > 40 mPa and $|\zeta| > 13\ \mathrm{s}^{-1}$ for simulation RA1009A3. Note, each simulation in Table 1 is executed at least

Table 1
Main Characteristics of the Conducted Simulations[a]

Simulation ID	Domain size $L_x \times L_y \times L_z$ (m^3)	Number of grid points	Grid spacing (mm)[b]	Velocity boundary condition	*Ra*	Γ
RA1006A3	0.198 × 0.198 × 0.066	198 × 198 × 66	1 (1.69)	No-slip	10^6	3
RA1007A3	0.420 × 0.420 × 0.140	420 × 420 × 140	1 (1.31)	No-slip	10^7	3
RA1008A3	0.912 × 0.912 × 0.304	912 × 912 × 304	1 (1.05)	No-slip	10^8	3
RA1009A3	1.968 × 1.968 × 0.656	984 × 984 × 328	2 (0.83)	No-slip	10^9	3
RA1009A3*	1.968 × 1.968 × 0.656	984 × 984 × 328	2 (0.83)	Free-slip	10^9	3
RA1010A2	2.816 × 2.816 × 1.408	1,408 × 1,408 × 704	2 (0.65)	No-slip	10^{10}	2
RA1010A3	4.224 × 4.224 × 1.408	2,112 × 2,112 × 704	2 (0.65)	No-slip	10^{10}	3
RA1010A4	5.632 × 5.632 × 1.408	2,816 × 2,816 × 704	2 (0.65)	No-slip	10^{10}	4
RA1011A3	9.108 × 9.108 × 3.036	4,554 × 4,554 × 1,518	2 (0.52)	No-slip	10^{11}	3

DNS in the near-wall region (see Appendix B).
[a]The simulations conducted for the gird resolution study (see Appendix C) are not listed. [b]The values in brackets show the actually required grid widths for guaranteeing a perfectly resolved DNS in the near-wall region (see Appendix B).

twice, once for determining the correct standard deviations and once for detecting dust devil-like vortices based on the correct thresholds. An exception is RA1011A3. Here, two simulations are computationally too expensive and the thresholds are estimated instead (see remark b in Table 2).

In a post processing step, dust devil centers are combined to vortex tracks with the following procedure:

1. A dust devil center at the current time step is compared to all detected centers within the next three consecutive model time steps
2. Two vortex centers are connected if after a maximum of three time steps the position of the second center is not more than two grid points away from the first one
3. An additional criterion for connecting centers that might belong to the same track is that the vorticities must have the same sense of rotation at all-time steps of the track
4. Because neighboring centers can belong to the same vortex, some of them are ignored before track analysis. As soon as a center is within the radius of another (sub)vortex at the current time step, the weaker center (rated by the vorticity) is disregarded

Point 4 requires the vortex radius to be known. As in Giersch et al. (2019) and Raasch and Franke (2011), the vortex radius is determined from the tangentially averaged pressure drop distribution around each center. It is defined as the distance at which the absolute pressure drop is reduced to 50% of the core pressure. For further details on dust devil track analysis, the reader is referred to Giersch et al. (2019).

The radius of a vortex might be underestimated due to technical restrictions. The horizontal domain decomposition implemented for parallelization implies that each processor core has principal access to only

Table 2
Detection Thresholds and Lifetime Limits for the Simulations Mentioned in 1 [a,b]

	RA1006A3	RA1007A3	RA1008A3	RA1009A3	RA1010A3	RA1011A3[c]
$\lvert p^* \rvert$ (mPa)	10	16	23	40	70	100
$\lvert \zeta \rvert$ (s^{-1})	3	4	4.5	13	18	25
	RA1009A3	RA1009A3*	RA1010A2	RA1010A3	RA1010A4	RA1011A3
$\tau_{N_{max}}$	0.3	0.27	0.24	0.2	0.25	0.14

[a]The thresholds for RA1010A2 and RA1010A4 are the same as for RA1010A3 and the thresholds for RA1009A3* are the same as for RA1009A3. [b]Remarks on the lifetime limits are given at the end of this subsection. [c]The listed thresholds are estimated values based on the simulations with lower Rayleigh numbers.

grid point data of a subdomain of the total domain. In order to calculate the radius for cases where the vortex center is situated near subdomain boundaries, data of directly adjacent subdomains are required, and are fetched from the respective neighboring cores before calculation. Due to technical restrictions (memory requirements and long data transfer times), data from nonadjacent subdomains are not considered. This means that vortices larger than the subdomain size might not be detected correctly. Increasing the subdomain size to be able to capture dust devils of any size is not a solution, because it would significantly increase the wallclock time of the simulations and would cause the core memory limit to be exceeded. As a compromise, subdomains with 24 grid points along x and y are used so that vortices that extend over more than this distance might not correctly captured. This problem is referred to as the "radius restriction."

Similar to previous dust devil studies (e.g., Giersch et al., 2019; Raasch & Franke, 2011), the statistical focus is on the dust devil maximum values regarding the absolute pressure drop $|p^*|_{\max}$ and vertical vorticity $|\zeta|_{\max}$ at the center, as well as the tangentially averaged horizontal $\{u_h\}_{\max}$, vertical $\{w\}_{\max}$, radial $\{u_{rad}\}_{\max}$, and tangential velocity $\{u_{tan}\}_{\max}$. The index "max" refers to the highest value during the lifetime of a specific vortex. $\{\cdot\}$ indicates the maximum of a tangentially averaged value around the dust devil center. The total number of detected dust devil-like vortices N, their lifetime τ, mean translation speed $\overline{v_t}$, and mean radius $\overline{r}$ will also be discussed. The overbar $\overline{\cdot}$ represents a value averaged over the lifetime of a single vortex.

Only long-lived vortices are considered in the statistics for two reasons. First, dust devils with a short lifetime are of less interest because their contribution to the overall transport of heat and dust are negligible compared to the long-lived vortices; and second, short lifetimes often do not allow for a well-developed vertical vortex, resulting in strong deviations from the typical circular shape. Therefore, only dust devils with a lifetime of

$$\tau > \max\left(\frac{2\pi\overline{r}}{\overline{\{u_{tan}\}}}, \tau_{N_{max}}\right) \tag{7}$$

are analyzed. Here, $\overline{\{u_{tan}\}}$ is the mean tangential velocity. The first constraint of Equation 7 restricts the statistics to vortices that allow an air parcel flowing with $\overline{\{u_{tan}\}}$ to circulate the vortex once or more during its lifetime. This restriction is referred as the "velocity constraint." $\tau_{N_{max}}$ is defined as the lower limit of the bin having the highest number of detected vortex tracks in the lifetime frequency distribution. An example histogram of the lifetime frequency distribution from simulation RA1010A3 is displayed in Figure 1. By convention, the axes are logarithmically scaled with an interval or bin size ratio of about $\sqrt{2}$ on the x-axis (e.g., Giersch et al., 2019; R. D.; Lorenz & Jackson, 2016). The number of vortex tracks decreases with increasing lifetime and the lifetime distribution indicates a relatively strong positive skew, which is typical for dust devil statistics derived from observations and numerical simulations (e.g., Giersch et al., 2019; R.; Lorenz, 2011; R. D.; Lorenz & Jackson, 2016; Nishizawa et al., 2016). The bin counts are fit by a truncated power law, which starts at the mode bin and is determined by using nonlinear least squares analysis. $\tau_{N_{max}}$ is equal to 0.2 s for run RA1010A3 and a differential slope (power law exponent) of −0.79 is calculated. The main purpose of the power law calculation is to enable quantitatively better comparisons with other dust devil studies.

The lifetime frequency distribution must be calculated for each simulation to filter out the short-lived vortices. The determined values for $\tau_{N_{max}}$ are listed in Table 2. As discussed in Section 3.3 below, the simulation RA1006A3 contains no dust devil-like structures. In simulation RA1007A3 only one vortex fulfilling the velocity constraint in Equation 7 is detected. Furthermore, RA1008A3 contains only 11 vortices, which is too sparse to calculate meaningful statistics. Therefore, no $\tau_{N_{max}}$ is set for these three simulations.

3. Results

The following section gives a general overview of the main characteristics of the simulations introduced in Section 2.1. This overview is mainly based on results derived from RA1010A3, the so-called control simulation. Afterward, the three-dimensional dust devil structure is analyzed and compared to LES results.

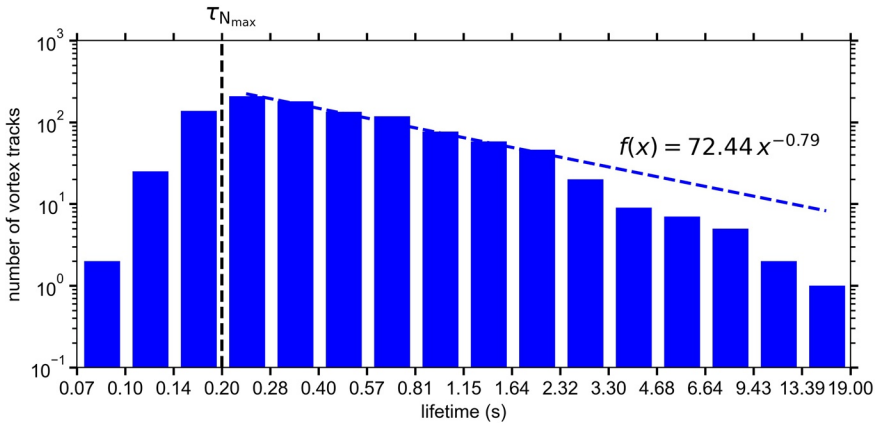

Figure 1. Number of vortex tracks fulfilling the velocity constraint of Equation 7 as a function of each track's lifetime for simulation RA1010A3. The labels on the *x*-axis demarcate the limits of each bin. The blue dashed line indicates a fitted power law with a slope of −0.79 using nonlinear least squares analysis. $\tau_{N_{max}}$ is marked by a black dashed line.

Finally, the setup for RA1010A3 is systematically modified to test the effect of the Rayleigh number, aspect ratio and surface friction on the dust devil statistics.

3.1. Control Simulation RA1010A3

The general flow features in RA1010A3 can be partly generalized to all other simulations performed in this study. For example, Figure 2 shows the change of horizontally and temporally averaged profiles of the potential temperature $\langle\theta\rangle_t$ and total sensible heat flux in vertical direction $\langle w\theta\rangle_t$ with time. The index *t* illustrates temporal averaging. Changes are marginal after 30 s. Therefore, a well-mixed bulk of the flow is reached after an initial spin-up of 30 s simulated time due to strong convection. The near-wall region is characterized through sharp temperature gradients because turbulent heat transport, and therefore mixing, drastically reduces in the vicinity of the plates. However, the exact value for the spin-up time increases with Rayleigh number from less than 10 s in RA1006A3 to about 30 s in RA1011A3. This increase directly follows from the vertical extent of the model domain, which is larger for higher Rayleigh numbers. As a consequence, the flow needs more time to mix up and to reach a statistically stationary state. If not otherwise stated, time averaging, indicated as $\langle\cdot\rangle_t$, henceforth refers to the dust devil detection and analysis period of 70 s, following spin-up. In a stationary state, the heat flux profile should be constant with height because in the horizontal average the temporal change of temperature only depends on the divergence of the vertical heat flux along *z*. Figure 2 indicates that stationarity appears after 30 s. The global time-averaged Nusselt number, a measure of the ratio between the total heat transport and heat conduction, is 136, which is well in the range of results from similar setups (e.g., Scheel & Schumacher, 2014; Shi et al., 2012; Stevens et al., 2010; Zou et al., 2019). For reference purposes, the large-eddy turnover time (for calculations see Sakievich et al., 2016) and Deardorff's convective velocity scale are also computed. The values for the control simulation are ∼20 s and 0.16 m s^{-1}, respectively. Both quantities decrease if the Rayleigh number is reduced.

Beside the height independent heat flux and the constant potential temperature values in the bulk of the flow with sharp gradients close to the plates (Figure 2), further typical flow features of RBC are reproduced (see also, De et al., 2017; Sakievich et al., 2016). An overview of the most relevant quantities is provided in Figure 3. Here, the horizontally and temporally averaged vertical profiles of variances of the horizontal velocity components and potential temperature have maximum values close to the bottom and top boundary with few changes in the bulk, whereas fluctuations of the vertical velocity component constantly increase away from the plates to a maximum in the middle part of the model domain. The averaged molecular contribution to the total sensible heat flux peaks at the plates and rapidly decreases to nearly zero in the bulk of the flow. For the turbulent heat flux, it is the opposite. The horizontal wind components have absolute values slightly above zero but with a more irregular structure. However, theoretically, zero values for the

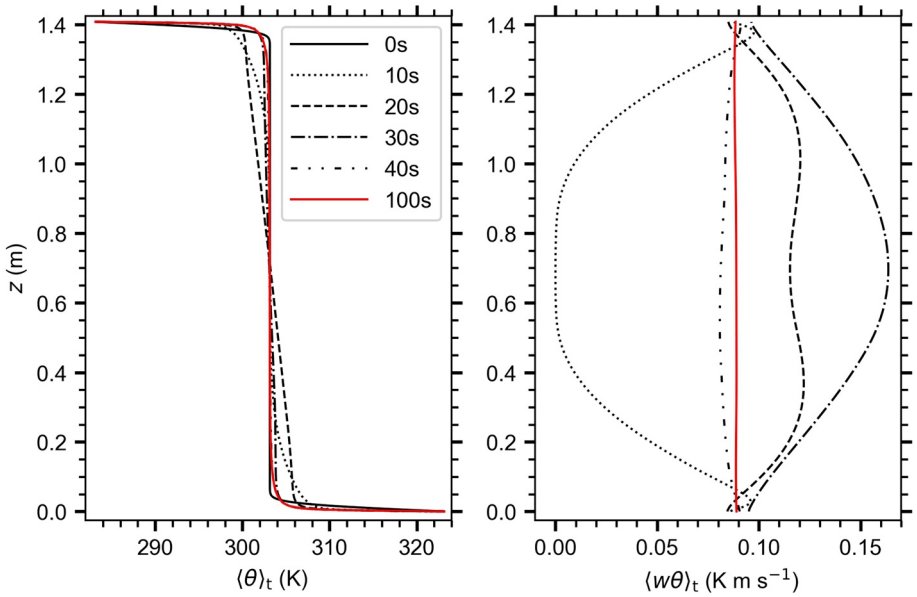

Figure 2. Horizontally and temporally averaged vertical profiles of the potential temperature (left) and total vertical sensible heat flux (right) for five different simulation times taken from RA1010A3. The black, broken curves show a 10 s average, whereas the red, solid lines indicate a 70 s (detection and analysis period for dust devils) average. The initial profile of the potential temperature is indicated by the solid black line. On the left, the line for 40 s simulated time is not apparent because it coincides with the 100 s (red) curve.

long-term averaged horizontal wind components should be assumed because no background wind is applied. This assumption is also valid because, on the one hand, the strength of the 70 s averaged horizontal flow components is only about 1% of the maximum fluctuations that occur in the flow ($\mathcal{O}(100\mathrm{cms}^{-1})$ in RA1010A3). On the other hand, the horizontal model extent of $2 \leq \Gamma \leq 4$ and averaging time of 70 s (roughly 67 times the free-fall time or 3 times the large-eddy turnover time in RA1010A3) are too small and short, respectively, to completely filter out the largest and most time-persistent structures that can exist in classical RBC (e.g., Pandey et al., 2018; Stevens et al., 2018). The magnitude of the horizontal wind derived from the averaged vertical profiles of u and v reaches its maxima slightly above/below the adjacent plate, with approximately constant positive values in between. However, because $\langle u \rangle_t$ and $\langle v \rangle_t$ can be approximated as zero, the horizontal wind defined as $\langle v_h \rangle_t = \sqrt{\langle u \rangle_t^2 + \langle v \rangle_t^2}$ is also negligible.

The boundary layer height $\delta_\theta = H/(2Nu_{\mathrm{wall}})$ is defined as the distance at which the linear extrapolation of the temperature profile from the wall equals the domain averaged temperature of 303.15 K (e.g., Belmonte et al., 1994; Shishkina et al., 2010). Nu_{wall} describes the horizontally and temporarily averaged Nusselt number at the wall. It is defined as

$$Nu_{\mathrm{wall}} = \frac{\left| \frac{\partial \langle \theta \rangle_t}{\partial z} \right|_{z=0}}{\Delta \theta H^{-1}}. \tag{8}$$

Figure 3 illustrates the well-known decrease of the scaled boundary layer height with the Rayleigh number (e.g., Hay & Papalexandris, 2019), which can be seen in the variance profiles of u, v, and θ by the shifted maximum in RA1010A3 compared to RA1007A3 (see zoomed profiles).

In horizontal cross sections of the vertical velocity, typical flow structures form pentagonal or hexagonal cells with narrow edges of high vertical velocity and broad centers with descending air. As discussed in Section 2 and 2.1, the occurrence of dust devils is likely directly connected to these structures. Figure 4 provides an overview of flow patterns changes in height and time. From top to bottom, three horizontal cross sections of the vertical velocity at different heights are displayed. The uppermost cross sections show the vertical velocity close to the lower thermal boundary layer height at 4 mm. The middle row of cross sections

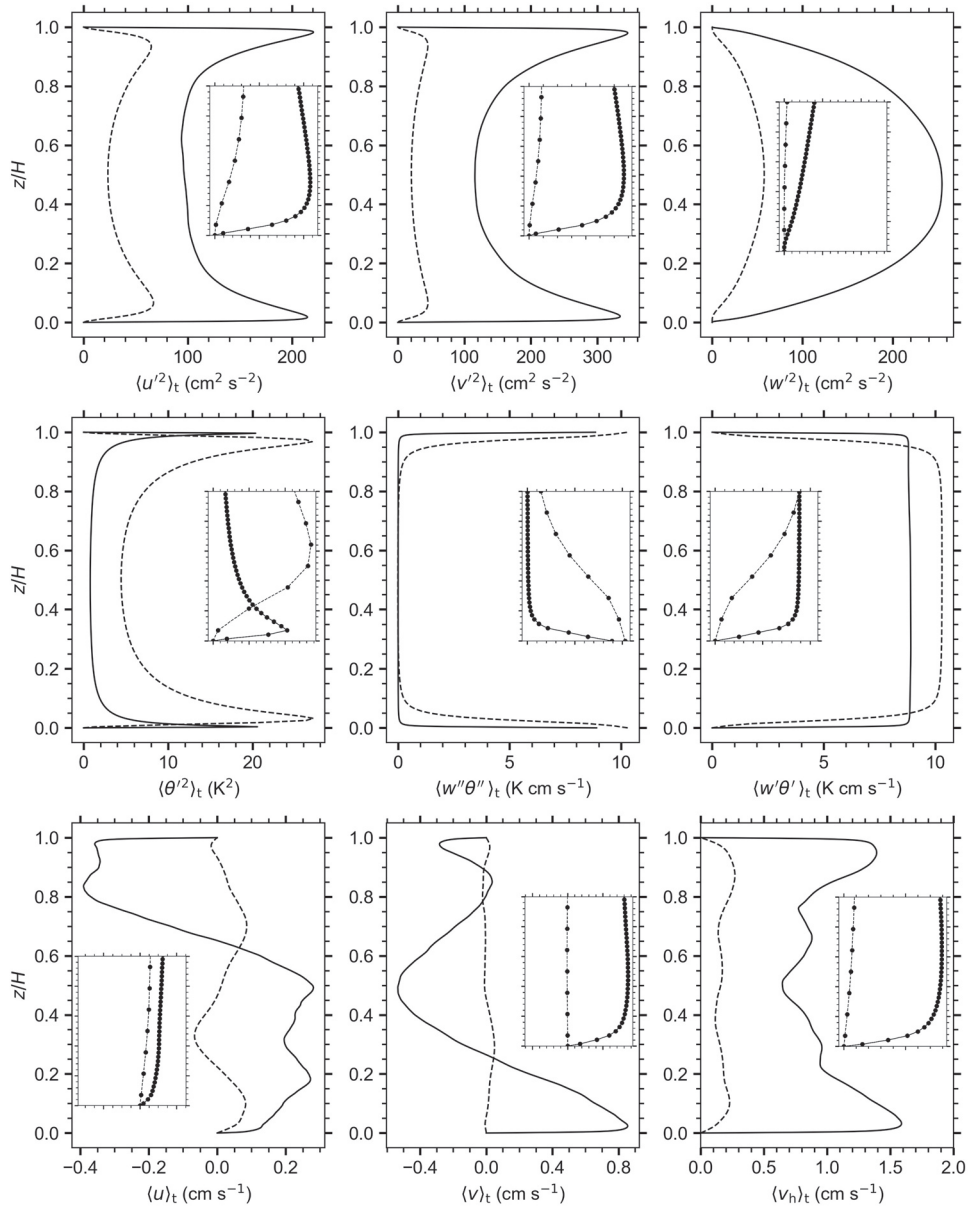

Figure 3. Horizontally and temporally averaged vertical profiles of variances (u'^2, v'^2, w'^2, θ'^2), molecular and turbulent heat fluxes ($w''\theta''$, $w'\theta'$), and horizontal wind velocities for simulation RA1007A3 (dashed lines) and RA1010A3 (solid lines). The horizontal velocity is defined by $\langle v_h \rangle_t = \sqrt{\langle u \rangle_t^2 + \langle v \rangle_t^2}$. In each inset, profiles of the near-wall region of the lower plate are magnified up to $z/H = 0.05$.

in Figure 4 are from well above the lower boundary layer but still quite close to the heated plate. The lowermost cross sections in Figure 4 are taken from the mid-plane. Additionally, from left to right, two snapshots of the vertical velocity at the beginning and end of the dust devil detection period are shown. Within the boundary layer close to the surface, structures are very small. This is reminiscent of results from other DNS studies on RBC (e.g., Mellado, 2012; Shi et al., 2012; Stevens et al., 2018; van Reeuwijk et al., 2008). The near-surface structure develops from a uniform, honeycomb-like pattern during the spin-up phase (not shown) to a more irregular pattern, where the small hexagonal structures appear stretched and compressed by the diverging and converging of the flow. Also the large-scale pattern from above is visible at 4 mm, especially through long bands of clustered upward motion. These patterns are also the dominant structures at 100 mm. After 30 s, they clearly resemble the pentagonal or hexagonal cells often reported in LES of

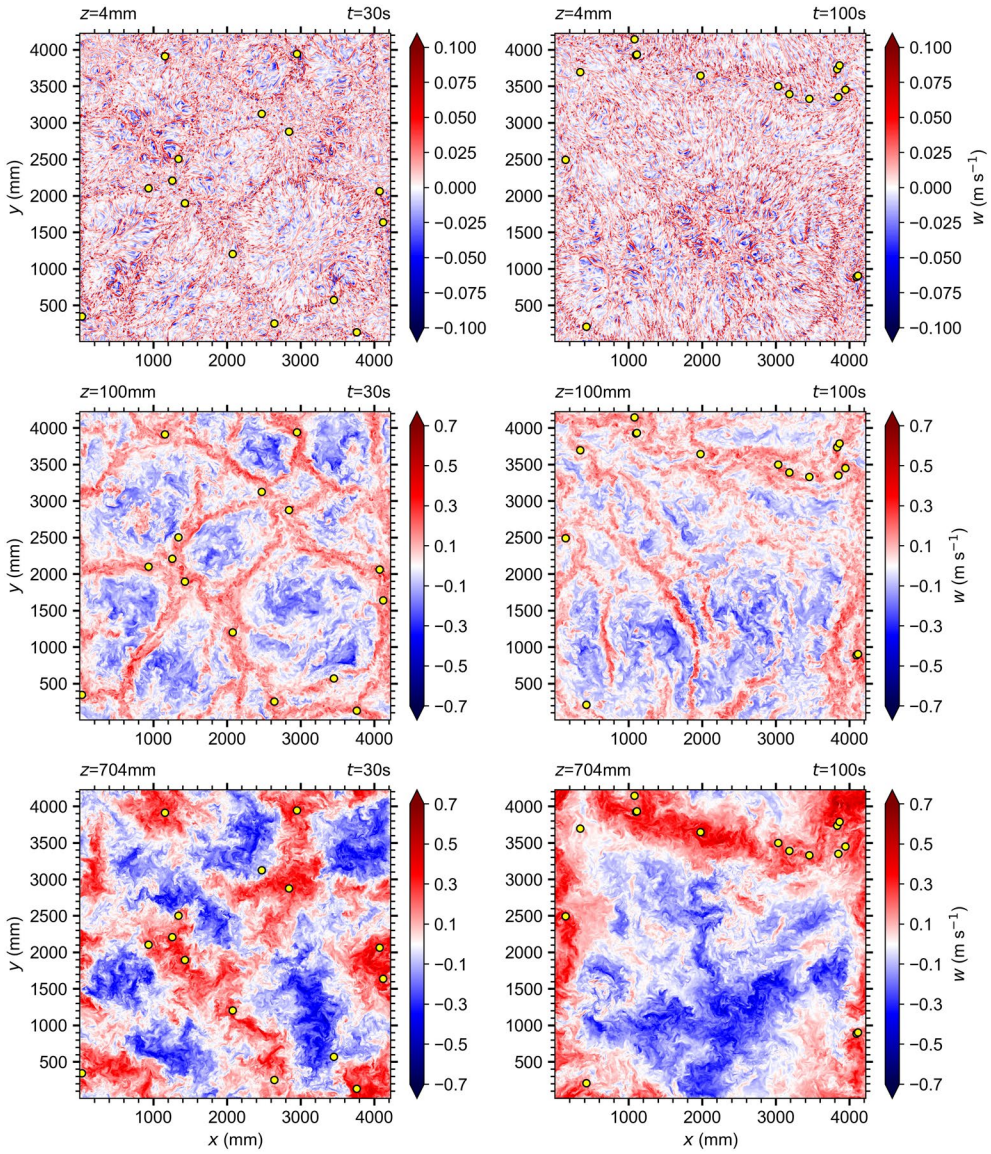

Figure 4. Horizontal cross sections of the instantaneous vertical velocity at 4 mm (top), 100 mm (middle), and 704 mm height (bottom) after 30 s (left) and 100 s (right) simulated time taken from simulation RA1010A3. Detected vortex centers at the first grid point above the surface are depicted as yellow dots. Note the different scale for $z = 4$ mm.

dust devils in the atmospheric boundary layer (e.g., Kanak, 2005; Raasch & Franke, 2011). DNS studies of RBC also show the occurrence of these forms in instantaneous flow fields (e.g., Bailon-Cuba et al., 2010). We call this state of the fluid the first flow regime. The hexagonal pattern at 100 mm disappears when its size matches the width of the computational domain. This happens in each simulation due to a broadening of the patterns. As a result, relatively long and narrow bands occur at later times (second flow regime), as exemplified in Figure 4 for 100 mm at the end of the simulation. Similarly, structures in the mid-plane grow to larger scales after 30 s simulated time. Starting from isolated plumes of ascending and descending air at 30 s, clustered regions with high- and low-vertical velocities develop. These regions are a consequence of merging plumes. That is why they appear much larger. The broadening process of structures until the horizontal domain size is reached is thoroughly discussed in Parodi et al. (2004), von Hardenberg et al. (2008), and Stevens et al. (2018). These publications suggest that an aspect ratio of 4 (our maximum) is still too low for capturing the finite horizontal saturation scale of the convection pattern. A minimum of 4π would be required to resolve this scale (von Hardenberg et al., 2008). However, it is critical to simulate high

Table 3
Dust Devil Properties at Detection Height Derived From Simulation RA1010A3[a]

N	T (s)	$\overline{v_t}$ (cm s^{-1})	$\overline{r}$ (mm)	$\lvert p^* \rvert_{max}$ (mPa)	$\lvert \zeta \rvert_{max}$ (s^{-1})	$\{u_{tan}\}_{max}$ (cm s^{-1})	$\{u_{rad}\}_{max}$ (cm s^{-1})	$\{w\}_{max}$ (cm s^{-1})
865	0.82 ± 1.21	15.3 ± 6.74	6.47 ± 3.13	255 ± 235	310 ± 125	32.8 ± 13.3	18.1 ± 7.76	13.5 ± 3.19
434↻/431↺	18.8	44.3	26.3	1,708	928	101	52.6	32.2

[a]The first row shows the population mean and standard deviation. The overall maximum values are displayed in the second row. For N, the number of clockwise and counterclockwise vortices is given.

Rayleigh numbers, rather than high aspect ratios, to achieve a sufficient count of dust devil-like vortices (see Section 3.3 and 3.4). Realizing both is currently not feasible due to limited computational resources. Note, dust devil statistics are not affected by the ongoing increase in cell size because statistical information about vortices derived from two different periods (30 to 65 s and 65 to 100 s) do not change significantly (not shown). The most crucial requirement for acquiring stationary statistics is to reach a well-mixed state of the flow. This requirement is satisfied before 30 s in every simulation.

Figure 4 depicts the location of detected dust devil-like vortices by yellow dots. As long as a coherent cellular pattern is visible at the lower part of the model domain (first flow regime), vertical vortices appear at cell edges and especially vertices, as already detailed by LES studies (e.g., Giersch et al., 2019; Kanak, 2005; Raasch & Franke, 2011). Once the size of the cells has reached the horizontal domain size (second flow regime), which occurs between 50 and 60 s in RA1010A3, dust devils persist and continue developing. During second flow regime, dust devils appear to be connected to the widest bands of high vertical velocities, where near-surface convergence is relatively strong (see cross sections for 100 and 704 mm at 100 s). These findings support the LES results of Raasch and Franke (2011), who also investigated the distribution of dust devil-like vortices in a domain that did not allow for the development of cellular flow structures due to the limited horizontal size. In their LES study, dust devil centers were also located along convergent bands of high vertical velocity.

The reasons for the preferred occurrence at certain locations in the flow pattern are summarized well by Raasch and Franke (2011). Their explanations can be applied to both flow regimes. For the first one, this has already been done in Section 1.2. In the second flow regime, high vertical wind velocities occur at pronounced flow convergence zones indicated by long bands with upward motions. Along these bands, flow convergence is irregularly shaped, often having a significant wind component parallel to the band. By chance, the parallel wind component is opposite on both sides of the convergence line and an overall initial rotation is created. This might also explain the occurrence of dust devils along the cell edges in the first flow regime. A further explanation for the occurrence of vortices along the near-surface convergence lines is the so-called hairpin mechanism, which is highlighted in Renno et al. (2004) and Kanak (2005). Near-surface horizontal vorticity created by directional shear is lifted by the updraft along the convergence lines and a vortex loop forms. The apex of the loop thins and weakens as it rises. Finally, the vortex breaks into two vortices of opposite rotation. Normally, one of these vortices decays, leaving a single vertical vortex. However, this vortex is more unstable and infrequent than those created at the vertices of the cellular pattern (Raasch & Franke, 2011). In addition, the simulation results show that two vortices of opposite rotation are rarely created along the convergence zones of the convective cells. This makes the hairpin mechanism not very probable for the formation of vertical vortices studied here.

Bulk properties at detection height (first grid point above the plate) are presented in Table 3 for the control simulation RA1010A3. Parameters are described in Section 2.2. The first row describes an average over all N detected vortices. The second row shows the maximum values with respect to all 865 dust devils fulfilling Equation 7. For N, however, the number of clockwise and counterclockwise rotating vortices is displayed. Additionally, standard deviations from the sample mean are given.

As expected, there are nearly the same number of clockwise and counterclockwise rotating vortices because no force exists that prefers a direction of rotation. Atmospheric observations and LES simulations, where the Coriolis force is considered, suggest the same (e.g., Balme & Greeley, 2006; Kanak, 2006; Raasch & Franke, 2011). Most of the dust devil-like vortices have a lifetime of ∼1 s. This is relatively short-lived

compared to, for example, the large-eddy turnover time (roughly 20 s for RA1010A3). Nevertheless, due to the strongly skewed probability distribution of dust devil parameters, there are single events within the simulation time of 100 s where persistent vertical vortices develop. The three longest lifetimes are 18.84, 11.66, and 9.85 s. In the convective boundary layer of the atmosphere, large-eddy turnover times of ∼600–1,200 s occur (e.g., Rizza et al., 2013), while dust devils have a lifetime from seconds to minutes. This shows that atmospheric dust devils typically last for less than the large-eddy turnover time, which is supported by the dust devil-like structures studied here. The translation speed is in the range of the background turbulent velocities of the horizontal components close to the plates if the root of the u-variance is interpreted as a typical velocity fluctuation (see Figure 3). In addition, the horizontal size has maximum values of several tens of millimeters. However, due the radius restriction explained in Section 2.2, the mean values of 6.47 and 26 mm in Table 3 slightly underestimate the real mean radii. This can be inferred by the fact that 3% of all instantaneously detected radii from the investigated vortex tracks reach 48 mm (24 grid points), which is the maximum distance that is considered along each horizontal direction from the dust devil core during detection (see Section 2.2). The vortex strength measured through the pressure drop at the center is a factor of 1/100 smaller than values observed in dust devils in the planetary boundary layer, whereas the vorticity is a factor of 100 higher (e.g., Balme & Greeley, 2006; Giersch et al., 2019). Because vorticity is calculated across one grid spacing (see Section 2.2), it highly depends on the chosen resolution. Wind velocities are one order of magnitude smaller than measured and simulated dust devil velocities in the planetary boundary layer. As in other studies, the largest velocity component is the tangential, followed by the radial, and finally the vertical (e.g., Balme & Greeley, 2006; Giersch et al., 2019; Raasch & Franke, 2011). Note, the largest absolute values of vortex properties like pressure drops, vorticities, or velocities, might occur above the detection height (see next section).

3.2. Averaged Three-Dimensional Vortex Structure—A Comparison With LES

After discussing the effects of the Rayleigh number, the aspect ratio, and the velocity boundary conditions on the dust devil statistics, this section will briefly compare the simulated three-dimensional dust devil structure with LES results. According to Fiedler and Kanak (2001), a high degree of similarity between intense columnar vortices in convective layers explored with DNS and LES is expected.

Figure 5 exhibits time-averaged horizontal cross sections of the near-surface pressure, vorticity, velocity, and temperature fields around the vortex with the longest lifetime in simulation RA1010A3. The time-averaged horizontal and vertical cross sections around a vortex core as well as the transects in Section 3.5 are derived with the same procedure as described in Raasch and Franke (2011). The basis of this procedure is the sampling of different variables on a $31 \times 31 \times 100$ points ($x/y/z$) moving grid with the vortex center in its middle and the lowest grid point at the bottom boundary of the model. The structure in Figure 5 appears very similar to that observed in dust devil-like vortices simulated with LES (e.g., Kanak, 2005; Ohno & Takemi, 2010; Raasch & Franke, 2011; Spiga et al., 2016). In general, the pressure, vorticity, and vertical velocity fields exhibit an axially symmetric behavior with distinct maximum absolute values at, or close to, the center—the vorticity especially so. The near-surface convergent flow around the dust devil is counterclockwise and has a strong radial inflow that advects air from the surrounding into the dust devil. Actually, three tongues of warmer air are advected from west, north, and southeast into the vortex center where the maximum temperature is reached. A temperature increase of 2–3 K is found, which is well in the range of common core temperature excursions in atmospheric dust devils (Murphy et al., 2016). The mean radius of the vortex, here defined as the distance where the mean absolute pressure drop is reduced to 50% of the mean core pressure drop, is between 3 and 4 mm.

In contrast to the LES of Raasch and Franke (2011), the maximum vertical velocity is directly at the center, rather than outside of it. This difference is attributed to the different physical analysis heights. In Raasch and Franke (2011), cross sections were analyzed at a physical height of 1 m (first grid point above the surface). This is well above the diffusive wall layer, which is completely parameterized in LES. Figure 5 shows cross sections at the first grid point above the surface, which corresponds to a physical height of 1 mm. This height is well within the diffusive wall layer. Accordingly, differences in the three-dimensional dust devil structure are expected. At higher altitudes, 10 mm for example, our DNS results indicate maximum vertical velocities adjacent to the center. Time-averaged vertical cross sections of the example vortex are displayed in

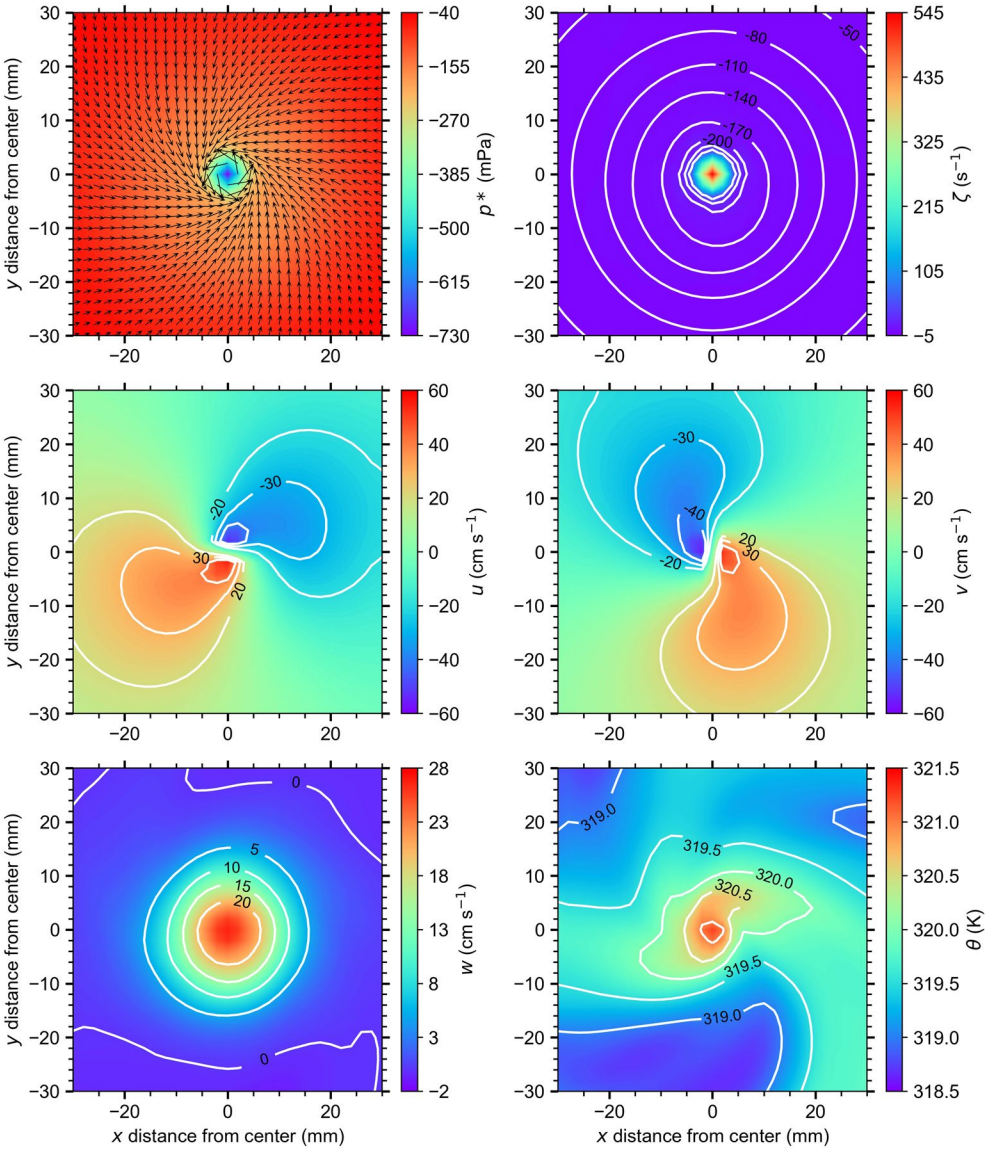

Figure 5. Time-averaged horizontal cross sections of the perturbation pressure, vorticity, velocities, and potential temperature at 1 mm height for the vortex with the longest lifetime derived from simulation RA1010A3. Additionally, vectors of horizontal velocity are shown in the pressure cross section and isolines of constant pressure are displayed in the vorticity field.

Figure 6. As in Raasch and Franke (2011), two isolated maxima to the left and right of the center occur. In zoomed vertical cross sections up to a height of 40 mm (not shown), the flow structure becomes very similar to the flow in atmospheric dust devils depicted schematically by Balme and Greeley (2006, Figure 8) or that of Rotunno (2013, Figure 9b). Although features like a stagnation point and a downward flow well above the plate are not observed in the averaged fields, it is expected that they are observable in the instantaneous data (the averaging is done during the simulation and the instantaneous data are not stored). This is supported by the significant reduction of positive vertical velocity in the central region above 20 mm height. However, Balme and Greeley (2006) also stated that the reversal in flow might not be present at all (upward flow throughout dust devil). Also Rotunno (2013) highlighted a single-celled below and doubled-celled above vortex form for certain swirl ratios similar to the vortices studied here. An estimation of the swirl ratio for the averaged vortex structure in Figure 6 yields 0.2–0.3.

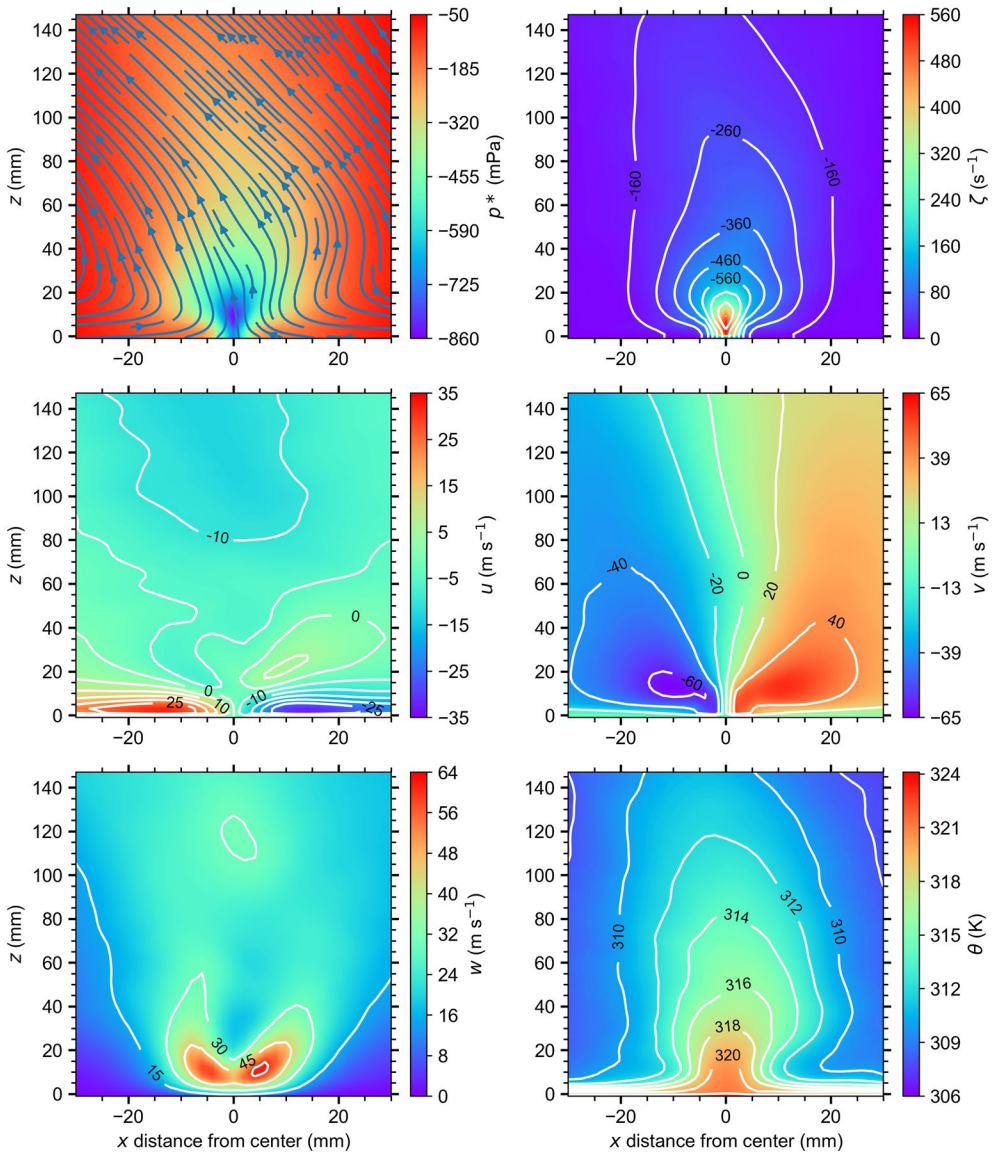

Figure 6. Time-averaged vertical cross sections of the perturbation pressure, vorticity, velocities, and potential temperature through the center for the vortex with the longest lifetime derived from simulation RA1010A3. Additionally, streamlines are shown in the pressure cross section and isolines of constant pressure are displayed in the vorticity field.

As in Raasch and Franke (2011), a time-persistent updraft at the vortex position that extends to the top of the mixed layer occurs. This is particularly evident in the streamlines of the pressure cross section and averaged vertical velocity displayed in Figure 6. However, the maximum upward motions occur within the lower region of the dust devil, whereas in Raasch and Franke (2011) vortices show the strongest time-averaged vertical velocities in their upper region. This inconsistency might be explained by the differences in the chosen setups. In the DNS of RBC, the domain is heated from below and cooled from above, resulting in both strong up- and down-drafts. In LES setups, where the convective layer is restricted by a temperature inversion, no cooling occurs. This lack of cooling could enable stronger and more persistent updrafts above the dust devil core, while in DNS of RBC updrafts could be partially suppressed by the cooling from the upper plate.

Regarding the general flow structure around the vortex, Figure 6 indicates that the inflow is restricted to the near-surface region (u-component). Conversely, the spiraling upward motion is visible up to 150 mm and

even above (v and w-component). This result is in agreement with the fluid dynamics discussion of atmospheric dust devils in Kurgansky et al. (2016), who also point out that the convergence of radial air flows is confined to the lowest part of the vortices.

Determining the height of a simulated dust devil is not trivial because of the potential vortex tilt and the absence of visible dust. For example, Gheynani and Taylor (2011), S. C. R. Rafkin et al. (2001), and Toigo et al. (2003) qualitatively estimated the height from the general flow pattern and vertical vorticity. Kanak et al. (2000) and Ohno and Takemi (2010) used information about the updraft region for their estimations. Raasch and Franke (2011) determined the vortex height based on the thresholds used for the detection of the vortex centers. However, Figure 6 indicates that the dust devil height depends on the quantity that is considered. If the same criterion as for the radius is used in vertical direction above the vortex center, a height of ∼50 mm (and therefore a height to diameter ratio of roughly 7) is obtained for the regarded vortex. This ratio is well in the range of atmospheric dust devils (e.g., Morton, 1966). Nevertheless, the other variables (e.g., v-component velocity, potential temperature) are significantly modified up to roughly 150 mm and even above.

Overall, the results presented here suggest that the main properties of dust devil-like vortices in DNS are very similar to those observed in nature and LES simulations.

3.3. Effects of the Rayleigh Number

To investigate the effect of the Rayleigh number on the dust devil statistics, simulation RA1010A3 is repeated with $Ra = 10^6$, 10^7, 10^8, 10^9, and 10^{11} (see also Table 1). Although the Rayleigh number is varied over five orders of magnitude, time-averaged vertical profiles, as indicated in Figure 3 and discussed in the previous section, remain mostly unchanged. Only the scaled height of the boundary layer decreases if Ra increases. The most relevant differences in the investigated flow features that are related to dust devils occur in the developing convective pattern.

The increase of cell size mentioned in Section 3.1 is not relevant for dust devil analysis for Rayleigh numbers less than 10^9 because the size already reaches the horizontal domain limit when the detection period starts after 30 s (not shown). This is due to the fact that the domain height is reduced for lower Rayleigh number cases, which also results in a smaller horizontal model extent (aspect ratios remain constant at $\Gamma = 3$). Thus, the fluid is always in the second flow regime during the dust devil detection and analysis period of 70 s if $Ra < 10^9$.

Furthermore, the appearance of structures changes significantly at every height if the Rayleigh number is modified by one order of magnitude or more. This is exemplified in Figure 7, where instantaneous cross sections of the vertical velocity are compared between RA1010A3 and RA1007A3. Cross sections were selected from heights within the boundary layer (4 and 4 mm, respectively; top row), above the boundary layer (100 and 25 mm, respectively; middle row), and from the vertical center of the model domain (704 and 70 mm, respectively; bottom row). A hexagonal pattern cannot be observed in simulation RA1007A3. This is also the case for simulation RA1008A3 and RA1006A3 (not shown). In addition, structures in the right column of Figure 7 are artificially enlarged because the axes scales are 1/10 of the left column due to a smaller model domain. The cross sections on the right can be seen as a smoother version of a zoomed sub-area of the respective cross section on the left. Because scale separation increases with Reynolds, and therefore Rayleigh number (e.g., Grossmann & Lohse, 2002; Wyngaard, 2010), the difference between the largest scales ($\mathcal{O}(1000\text{mm})$) in the mid-plane and the smallest scales in the boundary layer ($\mathcal{O}(1\text{mm})$) is quite large for $Ra = 10^{10}$ and much smaller in case of RA1007A3 ($\mathcal{O}(100\text{mm})$ and $\mathcal{O}(1\text{mm})$). Furthermore, the magnitude of the vertical velocity fluctuations decreases significantly with decreasing Rayleigh number because turbulent mixing is replaced by heat conduction at low Rayleigh numbers.

No dust devil centers are detected for simulation RA1007A3 at 30 s simulated time, which already suggests that the number of detected vortices reduces drastically at lower Rayleigh numbers. For example, results from RA1010A6 yield no vortex tracks at all, whereas at least 154 vortex tracks (3152 centers) are found for a Rayleigh number of 10^7. There is only a single vortex that fulfills our requirement on dust devil lifetime (Equation 7). In simulation RA1011A3, a total of 40,770 vortex tracks (2,358,967 centers) are detected.

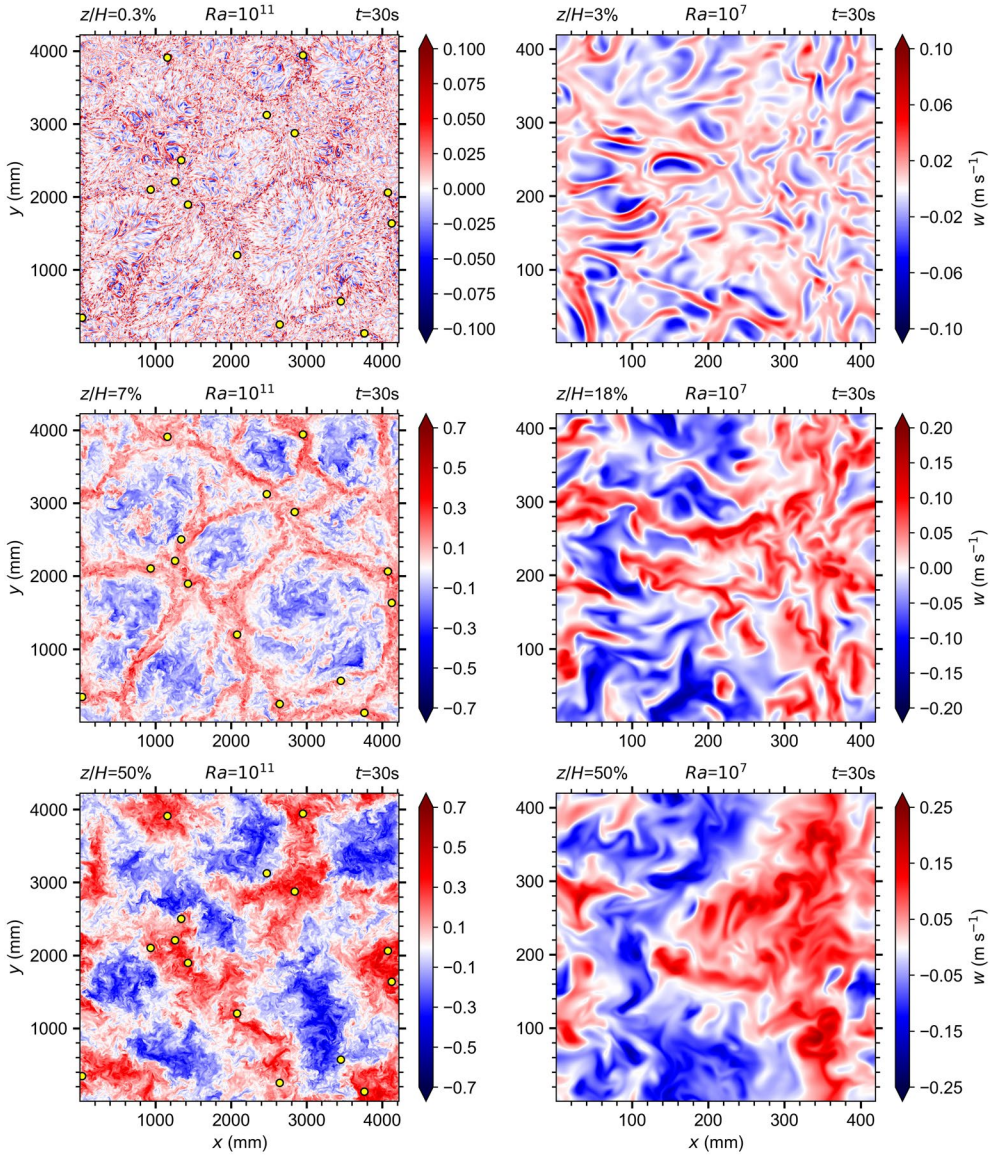

Figure 7. Horizontal cross sections of the instantaneous vertical velocity at three different heights after 30 s simulated time derived from RA1010A3 (left) and RA1007A3 (right). Detected vortex centers at the first grid point above the surface are depicted as yellow dots. Note the different scales. An explanation to the chosen heights is given in the text.

Therefore, a Rayleigh number of about 10^7 seems to be a minimum condition to identify dust devil-like vortices in numerical simulations of RBC. This Rayleigh number is consistent with the suggested value of 4×10^7 in Cortese and Balachandar (1993). For lower Rayleigh numbers, the scale separation and developing turbulence is not sufficient to create turbulent, time-persistent, coherent structures, such as dust devils. Hence, we are unable to derive meaningful dust devil statistics for $Ra \leq 10^8$. The number of detected vortices in RA1008A3 that fulfill Equation 7 is merely 11. For larger Rayleigh numbers, however, enough dust devil-like vortices are detected and analyzed to calculate bulk properties. The results are displayed in Figure 8, which shows the dependence of bulk vortex parameters on the Rayleigh number.

In total, 215, 865, and 3,834 dust devil-like vortices are recognized for RA1009A3, RA1010A3, and RA1011A3, respectively. The 95% confidence interval width in Figure 8 decreases with increasing *Ra* because the real population value is estimated from a much higher sample size. The increased formation of convective vortices for higher Rayleigh numbers is directly related to the more pronounced and stronger convective structures that develop as *Ra* becomes larger (see Figures 4 and 7). Furthermore, the higher the Rayleigh

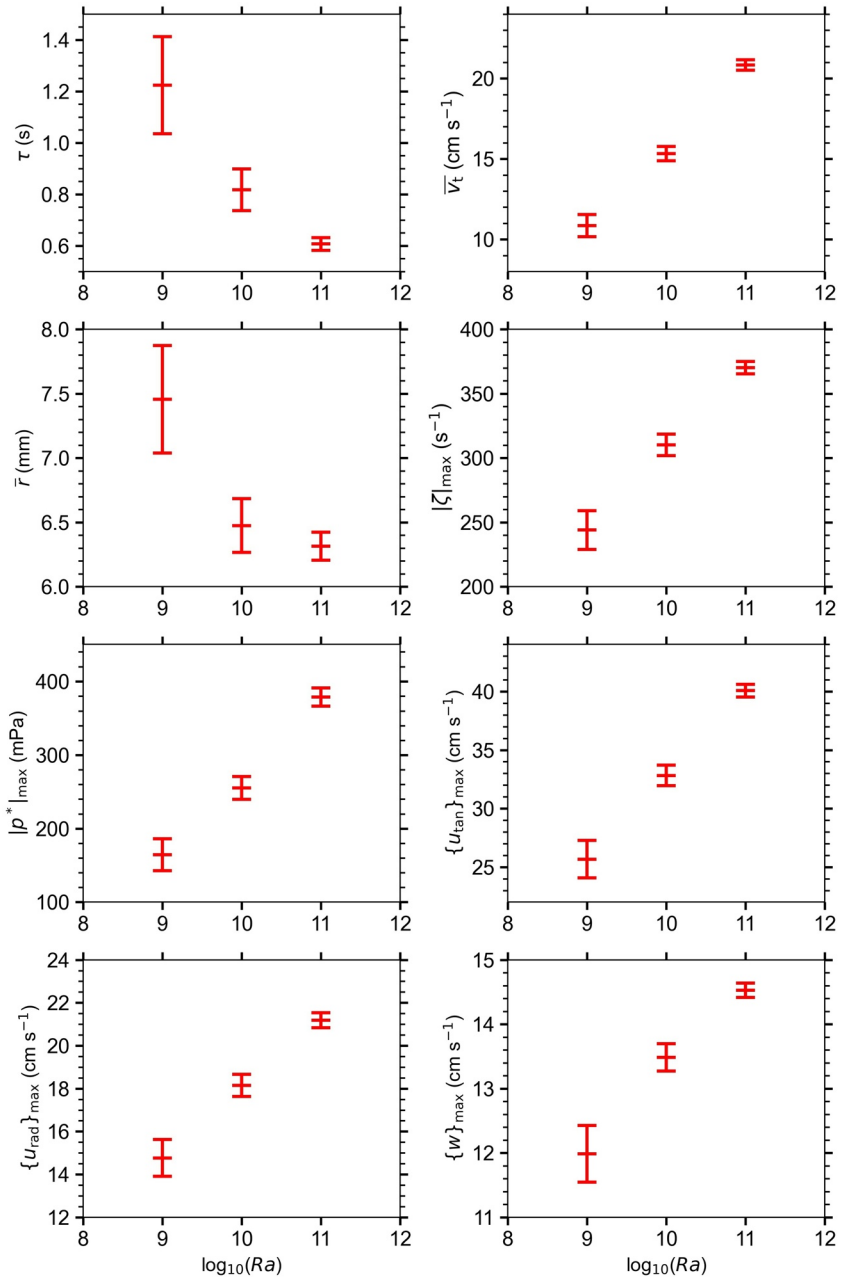

Figure 8. Dependence of dust devil characteristics on the Rayleigh number. Error bars (outer red lines) represent the 95% confidence intervals of the mean (middle red line). The mean is calculated over all *N* dust devils.

number, the higher the averaged dust devil strength, as indicated by increased maximum pressure drops, vorticities, and velocities. These increases are a consequence of stronger convective cells, which increase flow convergence and the twisting of horizontal vorticity, two mechanisms that are suggested to be mainly responsible for maintaining and strengthening the convective vortices (see Section 1.2). Stronger convection also causes higher background velocities and, by association, translation speeds as Rayleigh numbers increase. A parameter that decreases as *Ra* increases is the average lifetime. This is not the case because of a reduced number of long-lived dust devils, but rather due to an increased percentage of short-lived vortices in the entire sample. Hence, it seems that stronger turbulence especially favors the development of short-lived vortices and increases the probability of the initial development of coherent structures, like dust devils. Similar results were derived from LES by Giersch et al. (2019).

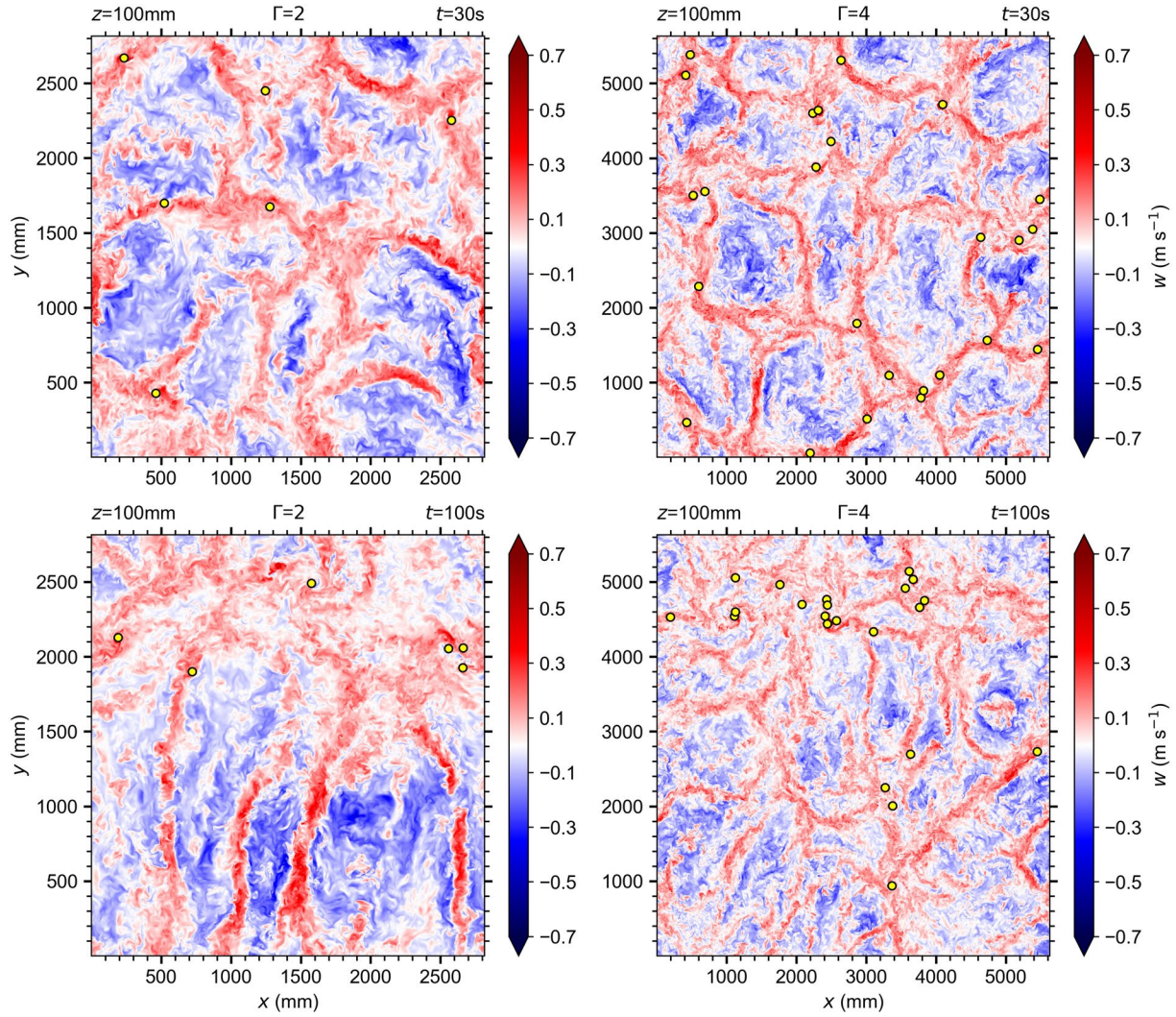

Figure 9. Horizontal cross sections of the instantaneous vertical velocity at 100 mm height after 30 s (top) and 100 s (bottom) simulated time taken from simulation RA1010A2 (left) and RA1010A4 (right). Detected vortex centers at the first grid point above the surface are depicted as yellow dots.

Ultimately, no statistically significant conclusions are drawn from the lifetime-averaged radii because the uncertainties are too high. First, the confidence intervals of the sample mean overlap between the two simulations RA1010A3 and RA1011A3. This overlap does not allow for a statistically significant conclusion. Second, the radius restriction explained in Section 2.2 increasingly influences the results for $Ra \geq 10^{10}$. The instantaneous radii of all detected vortex tracks in simulation RA1011A3 reach the numerical limitation of 48 mm in 8.43% of the cases, which is ∼5.1 and 6.7% more than for RA1010A3 and RA1009A3, respectively. This alone suggests that the portion of large dust devil-like vortices increases with *Ra*. However, the lifetime-averaged radius of a single vortex must not be affected by this because radius fluctuations can increase in both directions, toward higher as well as lower values, not modifying the mean. Therefore, an increased rate of vortex tracks that become instantaneously larger than the restricted detection range is not sufficient to draw any conclusions for the mean radius, especially because Figure 8 indicates exactly the opposite. Here, the mean radius averaged over all dust devils that fulfill our requirement on dust devil lifetime (Equation 7) decreases, at least from RA1009A3 to RA1010A3.

No linear correlation exists between vortex radius and core pressure drop, nor between the vortex radius and its duration. This absence of correlation is true in all performed simulations with both Rayleigh numbers larger than 10^8 and no-slip conditions. This is in agreement with the LES of Giersch et al. (2019). The Pear-

son correlation coefficients are ~0.2 or lower. For the core pressure drop and the duration, dust devil data show a moderate linear correlation with Pearson coefficients between 0.4 and 0.7. As expected from vortex theory, the strongest correlation is between the vorticity and the pressure drop, where coefficients of more than 0.9 are calculated.

In summary, for strong vertical vortices to frequently appear in the flow, Rayleigh numbers of at least 10^9 are necessary if an aspect ratio of 3 is used. This combination between a sufficiently large aspect ratio and Rayleigh number requires substantial computational resources that are presently available but have been largely prohibitive in the past (e.g., for RA1010A3, 105,000 core hours are necessary). The huge amount of computing power is one of the reasons why no comprehensive DNS study of dust devil-like vortices exists so far.

3.4. Effects of the Aspect Ratio

Previous studies (e.g., Giersch et al., 2019; Kanak, 2006; Raasch & Franke, 2011) and the results presented in Section 3.3 suggest that dust devil-like vortices are connected to specific patterns that develop in buoyancy-driven flows. Because these patterns depend on the chosen aspect ratio (e.g., Bailon-Cuba et al., 2010; Stevens et al., 2018; van der Poel et al., 2012), this section will clarify if the dust devil statistics also depend on the horizontal width of the model domain. Two additional simulations with an aspect ratio of 2 and 4 (RA1010A2 and RA1010A4) are performed and compared with the control simulation RA1010A3 for this purpose. Figure 9 displays how structures change with aspect ratio. For higher ratios, more cells exist at the beginning of the dust devil detection period. Consequently, more dust devil-like structures occur at the vertices and branches of these cells. The size of the cellular pattern increases and vanishes by $t = 100$ s in RA1010A2 because the horizontal scale of the largest structures exceeds the model domain size. For higher aspect ratios, this happens later than for lower ones. In case of $\Gamma = 4$, cellular structures are still apparent at $t = 100$ s, though they are much more distorted compared to $t = 30$ s. After the cells have grown to sizes comparable to the domain extent, vertical vortices occur within regions of clustered high vertical velocities. Similar to the vertices of the cellular pattern, these clusters are associated with points where several band-like structures merge and dust devils are recorded, which again supports the dust devil formation hypothesis of Raasch and Franke (2011) (see Section 1.2). The merging is especially apparent in the case with $\Gamma = 4$. Here, more of these points can be identified compared to RA1010A2, which results in a higher number of detected vortices in RA1010A4. However, the case with $\Gamma = 4$ is also unable to appropriately capture the time-persistent, large-scale cellular pattern after the initial growth period of the cells (several tens of seconds).

Consistent with previous studies (e.g., Bailon-Cuba et al., 2010; van der Poel et al., 2012), a transition from a single circulation to a multiple circulation system occurs if the aspect ratio increases. Figure 10 shows vertical cross sections of the instantaneous vertical velocity taken from the center of the model domain. In RA1010A2, there is only one large-scale circulation with an updraft at the center, whereas RA1010A4 has a two-circulation form. Even three-circulation forms occur at points during simulation RA1010A4. They also exist in the time-averaged flow field (not shown). Their diameters are comparable to the domain height and they develop a wide variety of structures depending on their y-positions. As indicated in Figure 9, the location of dust devils is connected to strong updrafts. In principle, this is supported by Figure 10, where a single dust devil center is detected by chance at the position of the output slice. The dust devil is clearly embedded in upward motions.

Regarding the dust devil statistics, no significant changes or trends are identified if the aspect ratio is varied between 2 and 4 except for the number of detected vortices, their mean translation speeds, and their maximum values of all other variables. In simulation RA1010A2, 353 vortices that fulfill our lifetime criterion (Equation 7) are detected. In RA1010A4, 1239 dust devil-like structures are found. Maximum values in RA1010A4 tend to be larger because the larger sample size increases the occurrence of extreme values. Additionally, larger aspect ratios increase the mean translation speeds from a population-averaged value of 14.21 $\mathrm{cm\,s^{-1}}$ (RA1010A2) to 16.12 $\mathrm{cm\,s^{-1}}$ (RA1010A4). The averaged translation speed in the control simulation (RA1010A3) is 15.33 $\mathrm{cm\,s^{-1}}$ (see Section 3.1). Interestingly, the instantaneous and time-averaged background velocities remain nearly constant between simulations with different aspect ratios (not shown). Therefore, higher translation speeds cannot be explained by an increase in background winds. It might be

that the translation speed is quite sensitive against the population size and that the real value is underestimated in case of low Γ.

After discussing the effects of the main control parameters in RBC, namely the Rayleigh number and the aspect ratio, on the dust devil statistics, the next section gives an insight on how the surface friction influences dust devil-like vortices.

3.5. Effects of Surface Friction

The importance of surface friction for the development of vertical vortices, such as tornadoes or dust devils, is addressed often in literature (e.g., Davies-Jones, 2015; Gu et al., 2010; Ito & Niino, 2013; Raasch & Franke, 2011; Roberts et al., 2016; Roberts & Xue, 2017). An overview of this topic is given in Kurgansky et al. (2016). In our simulations, the choice of velocity boundary conditions greatly influences the results. This section aims to highlight the effects of surface friction on dust devil-like vortices in DNS of RBC. For this purpose, simulation RA1009A3*, where free-slip boundary conditions are used, is performed and compared to RA1009A3.

Consistent with Ito and Niino (2013) and Mellado (2012), the overall convective pattern in RA1009A3* is similar to RA1009A3 except that stronger and more pronounced convergence lines at the cell borders arise close to the plates (not shown). Another difference is that the large-scale pattern well above the boundary layer is more dominant close to the plates if no surface friction is considered. Thus, structures inside the boundary layer and well above seem to be more strongly correlated. However, friction is not essential to generate dust devil-like vortices in the flow (see also Ito and Niino (2013)). In fact, simulation RA1009A3* produces 6,790 vortices–6,575 more than produced in RA1009A3 (215). This increased production suggests that the initial conditions for the development of vertical vortices are more favorable if surface friction is disabled. Because the initial formation process is not yet fully understood (e.g., Ito & Niino, 2013; Raasch & Franke, 2011; Renno et al., 2004), a rigorous explanation for this result is not be given here. It is possible that the overall initial vorticity is larger due to the stronger opposing and staggered flows toward the convergence lines at the borders and vertices of the convective cells near the ground (see also Section 1.2 and 3.1). In addition, the increased flow convergence alone, and consequently the vorticity concentration, provides more favorable conditions for vortex generation in simulation RA1009A3*. Mellado (2012) made similar observations of enhanced vorticity at the nodal points of the cellular network when free-slip, instead of no-slip, conditions are used.

The mean translation speeds and tangential, and consequently horizontal, velocities increase without surface friction, as well (see Table 4). The population-averaged value of $\overline{v_t}$ is 25 $\mathrm{cm\,s^{-1}}$ in RA1009A3* and 11 $\mathrm{cm\,s^{-1}}$ in RA1009A3. The translation speeds are higher due to the larger background velocities that occur in RA1009A3* because no frictional force exists that slows down the flow near the plates. The missing surface friction also explains the increase of tangential (and horizontal) velocities associated with dust devils in the case of free-slip conditions. Figure 11 illustrates this relationship. It shows horizontal transects at 1 mm height through the centers of two time-averaged, counter-rotating vortices that have the longest lifetime in their respective simulations RA1009A3 (vortex *A*) and RA1009A3* (vortex *B*). From the transects, it is clear that higher absolute tangential values are reached with free-slip conditions. This is additionally supported by Table 4. The value averaged over the vortex lifetime and subsequently over all detected dust devils ($\overline{\{u_{\tan}\}}$) yields an increase of ∼30%: from 17 $\mathrm{cm\,s^{-1}}$ in RA1009A3 to 22 $\mathrm{cm\,s^{-1}}$ in RA1009A3*. The laboratory study from Dessens (1972) also found a substantial increase of tangential velocities without surface friction.

Sinclair (1973) showed that the radial distribution of the tangential velocity of atmospheric dust devils can be approximated through a Rankine vortex described by

$$u_{\tan}(r) = \begin{cases} \omega r & \text{for } r \le R_0, \\ \dfrac{\omega R_0^2}{r} & \text{for } r > R_0. \end{cases} \tag{9}$$

Table 4
Dust Devil Properties at Detection Height Derived From Simulation RA1009A3 and RA1009A3[a]*

N	τ (s)	$\overline{v_t}$ (cm s^{-1})	$\overline{r}$ (mm)	$\lvert p^*\rvert_{max}$ (mPa)	$\lvert\zeta\rvert_{max}$ (s^{-1})	$\overline{\{u_{tan}\}}$ (cm s^{-1})	$\overline{\{u_{rad}\}}$ (cm s^{-1})	$\overline{\{w\}}$ (cm s^{-1})
215	1.22 ± 1.4	10.9 ± 5.08	7.46 ± 3.1	164 ± 161	244 ± 112	17.2 ± 4.71	11.1 ± 3.63	8.36 ± 1.6
98↻/117↺	8.57	29.1	19.7	1158	753	42.5	25.6	13.2
6790	0.73 ± 0.49	24.8 ± 10.1	6.12 ± 2.28	107 ± 59.4	164 ± 46.2	21.8 ± 4.97	9.92 ± 2.77	1.88 ± 0.46
3422↻/3368↺	5.26	59.6	28.5	519	391	45.5	23.7	5.13

[a]The first row shows the population mean and standard deviation. The overall maximum values are displayed in the second row. For N, the number of clockwise and counterclockwise vortices is given. The upper part shows the data for RA1009A3 and the lower part RA1009A3*. Here, lifetime-averaged velocities are displayed because they reveal a more obvious trend than the maximum values.

here, $\omega = \zeta/2$ is the constant angular velocity. r describes the distance from the center and R_0 the location where u_{tan} becomes maximum. In Figure 11, Rankine profiles are displayed for vortex A and B under the assumption that ζ is equal to the central value (225 s^{-1} and −176 s^{-1}) and that R_0 can be described by the mean distance from the center where $\{u_{tan}\}$ occurs (3.52 and 5.43 mm). In addition, a perfectly symmetric dust devil is assumed. It is evident, that vortex A and B can be approximated by the Rankine vortex model similar to atmospheric dust devils (Sinclair, 1973). However, the model tends to overestimate the tangential velocities, especially in the vicinity of R_0. This is also observed for atmospheric dust devils (Sinclair, 1973). The overestimation has several reasons. The Rankine vortex model does not take into account the friction force and, consequently, neglects the radial inflow. In addition, the model assumes a constant vorticity within the core region. For vortex A and B, the vorticity is approximated by the mean value in the center. There, ζ reaches its maximum. Also R_0 contains uncertainties. In the Rankine model, R_0 is the position where u_{tan} becomes maximum and where the total pressure deficit reaches 50% of its central value. For vortex A and B, however, these positions are not the same and it has to be decided which value is taken for Equation 9. Therefore, there might be a combination of ζ and R_0 that fits the tangential velocities shown in Figure 11 even better. The above mentioned values for ζ and R_0 enable together with the Rankine model an estimation of the core pressure drop using $\rho\omega^2 R_0^2$. With $\rho = 1$ kg m^{-3} a value of 156 mPa for vortex A and 229 mPa for vortex B is calculated. This corresponds well to the actually simulated range of p^* close to the vortices' core (100–200 mPa). The similarity of the detected vortices to the Rankine vortex model confirms again that they are similar to atmospheric dust devils (see also Section 3.2).

Table 4 indicates that the absolute radial and vertical velocities of the vortices close to the vortex core tend to be smaller if no surface friction is considered. The decrease in the mean radial ($\overline{\{u_{rad}\}}$) and vertical ($\overline{\{w\}}$) component is about 10% and 80%, respectively. These findings are additionally supported by Figure 11. The time-averaged vertical velocity is nearly zero for the vortex extracted from simulation RA1009A3* (vortex B). Instead, vortex A shows much higher vertical velocities of ∼10 cm s^{-1}, especially near the center. The transects of the radial velocity show a completely different behavior, however. Vortex A displays the expected constant and symmetric inflow along the center (positive u_{rad}), while vortex B shows an inflow at the left and an outflow at the right side of the vortex core indicated by a change of sign. Figure 12, where time-averaged horizontal cross sections of the perturbation pressure together with vectors of the horizontal flow field are shown, clarifies this behavior. The horizontal flow along the transect at $y = 0$ mm is continuously directed in the positive x-direction for vortex B. Therefore, u_{rad}, defined as positive if there is an inflow into the vortex core, must change its sign in Figure 11.

From a fluid dynamics perspective, the dependency of the dust devil radial and vertical velocity component on the velocity boundary conditions is explained as follows. The wind around the vortices results from a balance of the pressure gradient, centrifugal, and frictional force, whereas the friction is responsible for creating the radial inflow into the vortex (see also Kurgansky et al., 2016). The result is a pronounced, rotating inflow into the vortex center and a single, well-defined vortex is created, as illustrated in Figure 12 (left). Due to the incompressibility of the flow, the air must move upwards and high vertical velocities occur in the central region. However, if no friction at the plates is considered, no radial inflow develops and the vortex is described by the cyclostrophic balance, which explains the reduced radial and vertical velocities in RA1009A3*.

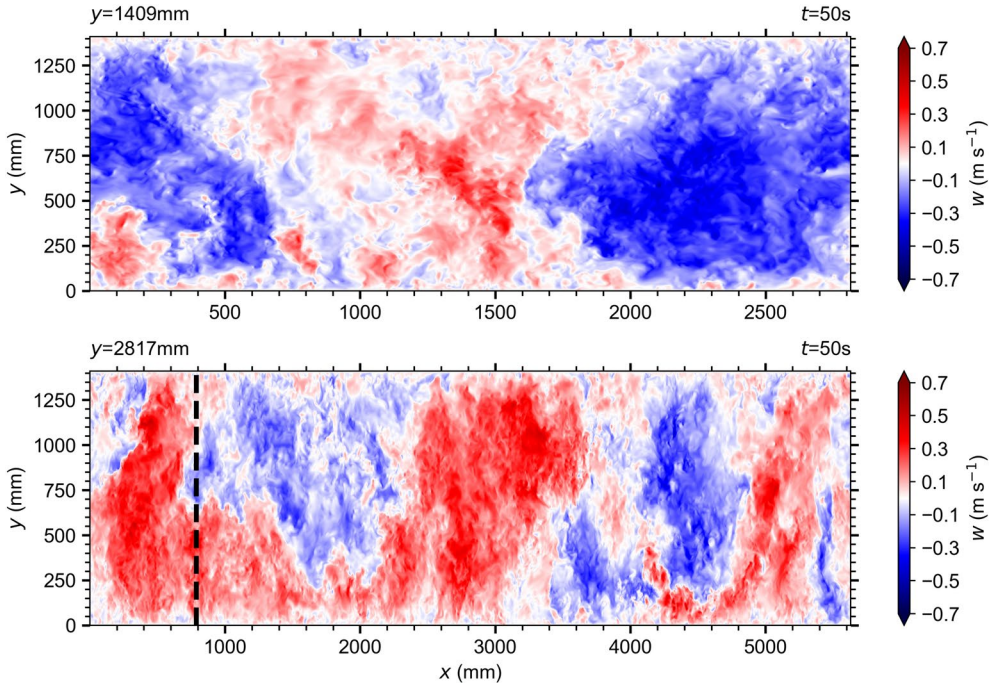

Figure 10. Vertical cross sections of the instantaneous vertical velocity at the center after 50 s simulated time taken from simulation RA1010A2 (top) and RA1010A4 (bottom). The black line indicates the position of a dust devil center defined at the first grid point above the bottom surface.

Furthermore, the size of vortices increases under no-slip conditions (see Figure 12). It is obvious that the vortex A influences the entire horizontal flow, whereas the vortex B is more concentrated. The size increase is additionally supported by the lifetime-averaged radius ($\overline{r}$), which has a population mean of 7.46 mm in the case of no-slip conditions and 6.12 mm if free-slip conditions are used. These results are consistent with results from Wilkins et al. (1975), who also found larger vortices formed in the friction layer.

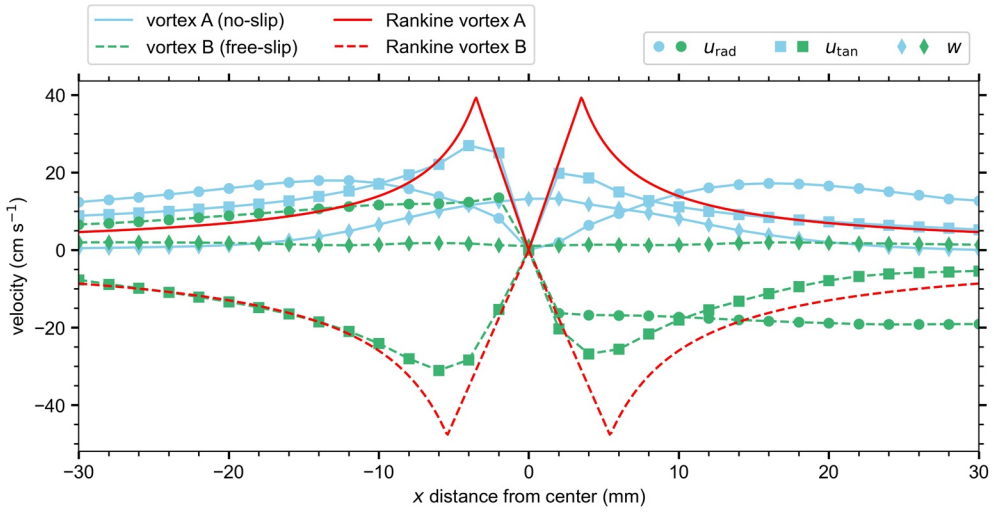

Figure 11. Horizontal transects at 1 mm height through the centers of the time-averaged vortices with the longest lifetimes. Blue solid lines describe the velocities for the vortex in RA1009A3 (vortex *A*), whereas green dashed lines indicate the velocities for the vortex in RA1009A3* (vortex *B*). Circles indicate radial (u_{rad}), squares indicate tangential (u_{tan}), and diamonds indicate vertical velocity (w). The radial velocity is defined as positive toward the center and the tangential velocity is defined as positive in the counterclockwise (cyclonic) direction. Red lines illustrate profiles according to the Rankine vortex model.

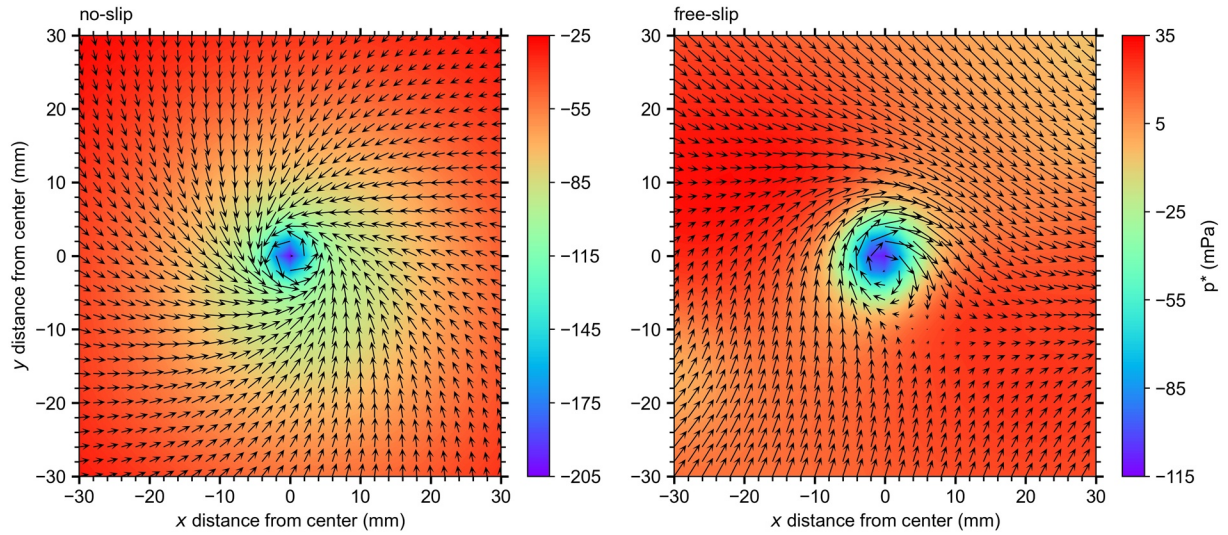

Figure 12. Time-averaged horizontal cross sections of the perturbation pressure at 1 mm height for the vortex with the highest lifetime derived from simulation RA1009A3 (left, vortex *A*) and RA1009A3* (right, vortex *B*). Note the different scales. Additionally, vectors of horizontal velocity are shown.

The pressure drop associated with vortex formation is larger with surface friction, an effect that has already been reported by Zhao et al. (2004). Figure 12 highlights this finding for the single vortices *A* and *B*. Vortex *A* has a mean core pressure drop of −202 mPa, whereas vortex *B* has a value of −110 mPa. In addition, the maximum pressure drop during the vortex lifetime averaged over all detected dust devils ($\overline{|p^*|_{\max}}$) increases by more than 50% from 107 mPa in RA101009* to 164 mPa in RA101009. Vorticity increases significantly if surface friction is considered because the vorticity correlate with the magnitude of the central pressure low.

The more intense vortices are explained by the budget equation for the vertical vorticity given in Section 1.2. As already discussed, the near-surface flow convergence in the vortex core is reduced under free-slip conditions due to the lower or even missing radial inflow (less vorticity concentration). Therefore, ζ_{div} contributes less to the generation and maintenance of vorticity. An analysis of the horizontally averaged ζ_{div} around the vortex core (11 × 11 grid points) at the second grid point above the surface yields absolute values between 200 and 2,500 s^{-2} during the lifetime of vortex A. Vortex B show values between 0 and 400 s^{-2}. Also, the horizontally averaged ζ_{twis} is much smaller for vortex B (0–100 s^{-2}) than for vortex A (100–1,400 s^{-2}) because there is less shear without friction. Both effects significantly decrease the vertical vorticity of the vortices and, consequently, the pressure drop in the center of vortex B. The remaining budget terms in Equation 1 causes an overall reduction of absolute vertical vorticity in both vortex centers. Low values of $|\zeta|$ are horizontally advected toward the core, high values are vertically advected upward away from the center, and molecular diffusion balances extreme values. The vertical advection in vortex B is much weaker (0–50 s^{-2}) compared to the horizontal (0–500 s^{-2}) due to low vertical velocities in the core. In vortex A, however, both advection terms are of similar size (100–1,000 s^{-2}).

A consequence of the reduced vertical vorticity increase through convergence and twisting is the reduced averaged lifetime under free-slip conditions. A vortex that develops under no-slip conditions has a mean lifetime of 1.22 s, which is about 70% higher than the averaged lifetime under free-slip conditions (0.73 s). Therefore, surface friction is important for maintaining vortices once they are created. The longest vortex lifetime in RA101009 is 8.57 s and is 5.26 s in RA101009*.

4. Summary and Conclusion

This study extensively investigated dust devil-like vortices using DNS of RBC for the first time. The special focus was on the effects of the Rayleigh number, aspect ratio, and surface friction on dust devil statistics. Previous studies mostly used LES to investigate vertical vortices in convective flows (e.g., Giersch et al., 2019;

Kanak, 2006; Raasch & Franke, 2011) or they analyzed dust devils as a side-note in their studies (e.g., Mellado, 2012). Especially, DNS results of dust devils in flows with Rayleigh numbers larger than 10^7 are lacking in the literature (see Cortese & Balachandar, 1993; Fiedler & Kanak, 2001; Iijima & Tamura, 2008).

After introducing the numerical methods and setups that were used, it was shown that dust devil-like vortices were frequently identified in a simulation, where a Rayleigh number of 10^{10}, an aspect ratio of 3, and no-slip boundary conditions were applied. The vertical vortices mainly occurred at the cell vertices and edges of the convective cells, similar to LES results (e.g., Giersch et al., 2019; Kanak, 2005). However, due to an increase in structure size up to the horizontal domain size, the cellular pattern disappeared over time. Dust devil-like structures preferentially occurred in regions, where strong near-surface convergence lines were clustered. This is in agreement with Raasch and Franke (2011), who also investigated dust devils in a domain that was too small to allow for an undisturbed development of the cellular pattern. However, their statistics were not influenced by the broadening effect.

DNS results were compared to existing LES data with focus on the three-dimensional structure of dust devil-like vortices. Dust devils simulated with DNS and LES displayed similar results. Only differences in the distribution of the vertical velocity around the vortex center arose, which were attributed to the discrepancies of the underlying setups that were used to investigate dust devils with DNS and LES. The similarity of results suggests that there is no need to explicitly resolve the small-scale turbulence near the ground and that the surface layer parameterizations in LES do not have a dramatic effect on the simulated dust devil-like structures. The results from LES are reliable if a sufficiently small grid spacing is used. This is especially true for larger dust devils. However, the exact value of a sufficiently small grid spacing for acquiring converged, quantitative dust devil information is still unknown in LES. This grid spacing will be determined in a follow-up study in which nesting techniques enable LES with 1 m grid spacing and even lower.

One of the main control parameters in RBC that significantly influences flow properties and structures is the Raleigh number (e.g., Stevens et al., 2018). Our results suggested that a minimum Rayleigh number of 10^7 was necessary for the development of dust devil-like vortices, which is much less than the Rayleigh number in the atmosphere ($\sim 10^{18}$). Higher values increased the number of detected vortices significantly, from one single vortex in the simulation with $Ra = 10^7$ to 3,834 vortices in the run with $Ra = 10^{11}$ (70 s detection time). In addition, the higher the Rayleigh number, the higher the translation speeds and dust devil intensities, which were accompanied by an increase in pressure drop, vertical vorticity, and velocity. However, the averaged lifetime of dust devils decreased if the Rayleigh number increased. Nevertheless, long-lasting vertical vortices of around 10 s still developed.

Another parameter known to significantly modify flow properties in RBC is the aspect ratio (e.g., Bailon-Cuba et al., 2010). Due to limited computing power, only aspect ratios between 2 and 4 were addressed in this study. Our results, as well as the results from previous studies (e.g., Stevens et al., 2018; von Hardenberg et al., 2008), showed that even an aspect ratio of four was far from able to resolve large-scale convective patterns in RBC. Dust devil statistics were established for each aspect ratio. Interestingly, no statistically significant effect of the aspect ratio on most of the vortex properties was identified, although large-scale flow circulations were captured more realistically within larger model domains. Only the number, averaged translation speed, and probability for very strong dust devils increased. These findings, except the relation between aspect ratio and translation speed, were directly attributed to the larger horizontal domain for higher aspect ratios.

Velocity boundary conditions are still being researched in connection with convective vortices due to the potentially high influence of friction on the vortex properties (e.g., Gu et al., 2010; Raasch & Franke, 2011). Our DNS results confirmed the significant influence of surface friction. With free-slip conditions, the number of detected vortices increased by a factor of 30. Mean translation speeds and tangential velocities were higher by a factor of 2.3 and 1.3, respectively. However, because there was no surface friction, dust devil-like vortices were in approximately cyclostrophic balance, with reduced radial, and consequently, vertical velocities. Furthermore, lifetimes, radii, and intensities were much smaller under free-slip boundary conditions. Therefore, friction is essential for strengthening and maintaining dust devil-like vortices.

This study was a first step toward the simulation of dust devils with DNS. Additional influencing factors, such as the background wind or surface heterogeneities, were not regarded. It is expected that conclusions

would be similar to LES studies (e.g., Giersch et al., 2019; Kanak, 2005; Raasch & Franke, 2011) or field campaigns (e.g., Renno et al., 2004; Ryan, 1972; Sinclair, 1969). Furthermore, it is possible that the restricting domain size in this study had an effect on the dust devil statistics. For this reason, simulations with very high aspect ratios that allow for an undisturbed development of large-scale structures in RBC should be performed. High aspect ratios, together with extended simulation time, would further improve the dust devil statistics, as well. Nevertheless, the general effects of the Rayleigh number, aspect ratio, and surface friction on dust devils were shown clearly.

In follow-up studies, we will compare our DNS results to laboratory-like experiments that were performed on the same scale (Loesch & du Puits, 2020). The Barrel of Ilmenau, which is a large-scale experimental facility to investigate turbulent convection, and hence dust devil-like structures, is an appropriate environment for creating the experimental data (e.g., du Puits et al., 2013). The comparison will allow us to identify possible differences and reveal the weaknesses and strengths of each method used to analyze convective vortices. However, because our numerical results produced maximum horizontal vortex sizes on the order of several tens of millimeters, it will require some technical effort to detect dust devil-like vortices of such small scale in the laboratory.

Appendix A: Validation of PALM's DNS Mode

For the validation of the DNS mode, the setup NsD of Mellado (2012), who investigated free (unbounded) convection over a heated, rigid, and impermeable plate with the numerical model Tlab (https://github.com/turbulencia/tlab), is repeated with PALM. The setup requires constant buoyancy and no-slip boundary conditions for the velocities at the bottom. At the top, free-slip boundary conditions with Neuman conditions for scalars are used. To save computational costs, the simulation with $1{,}024 \times 1{,}024 \times 768$ grid points introduced in the appendix of Mellado (2012) is simulated. He demonstrated that this number of grid points is already sufficient to capture the physics of the setup realistically. However, the results, which are used here for comparison to the PALM data, are taken from the high-resolution NsD case published in the main part of Mellado (2012). The NsD setup from the appendix is defined through the so-called reference Rayleigh number

$$Ra_0 = \frac{b_0 L_0^3}{\nu\kappa} = 9 \times 10^8, \tag{A1}$$

where ν is equal to κ ($Pr = 1$) and is set to 1.76×10^{-5} m^2 s^{-1}. For the constant buoyancy at the surface b_0, a value of 0.40875 m s^{-2} is assumed. Setting the horizontal model extent L_0 to 0.88 m yields $Ra_0 = 9 \times 10^8$ as defined in Equation A1. The above mentioned number of grid points results in a resolution of 0.86 mm and a model height of 0.66 m. As in Mellado (2012), the simulations are stopped when the boundary layer thickness is equal to about $0.3L_0$ to avoid finite-size effects on the results. During initialization of the model, zero velocities and a strong unstably stratified layer close to the bottom plate with neutral stratification above are assumed. The initial potential temperature profile is constructed using the error function similar to Equation 5 but without assuming symmetry. The only real difference in the NsD setup compared to Mellado (2012) is the way how horizontal perturbations are initiated to trigger off convection at the beginning of the model run. Mellado (2012) applied initial broadband perturbations to the buoyancy field, whereas in the PALM setup uniformly distributed random perturbations are imposed on the horizontal velocities.

For evaluating the validation run NsD, the temporal evolution of the scaled gradient thickness δ_g^+ is considered. If not otherwise stated, symbols, variables, and scaling are the same as in the original publication of Mellado (2012). δ_g^+ contains all mean surface properties in one quantity and can be seen as a measure of the diffusive wall layer thickness (Mellado, 2012). In addition to δ_g^+, the vertical profiles of the scaled molecular and turbulent contribution to the overall heat flux at the end of the simulation are discussed. All quantities are displayed in Figure A1. The δ_g^+ curves are very similar. In both cases, a maximum right after the start of the simulation occurs, combined with a rapid decrease afterward, and followed by a slight increase until the end of the simulation. The only difference is the initial transition to a near-steady behavior, marked by the initial overshooting of δ_g^+ and the subsequent decline, which takes more time in the PALM simulation.

This might be attributed to the different ways in which perturbations are imposed on the flow at the beginning of the runs. Mellado (2012) imposed initial perturbations on the buoyancy field by using a random field characterized by a zero mean value and a Gaussian power spectral density centered at some given spatial frequency. Thus, more energy could be explicitly distributed into the smaller scales, where dissipation is maximum. This procedure allows a more rapid development into a steady-state compared to imposing random perturbations on the velocity field by using uniformly distributed random numbers, as it is done by default in the PALM simulation.

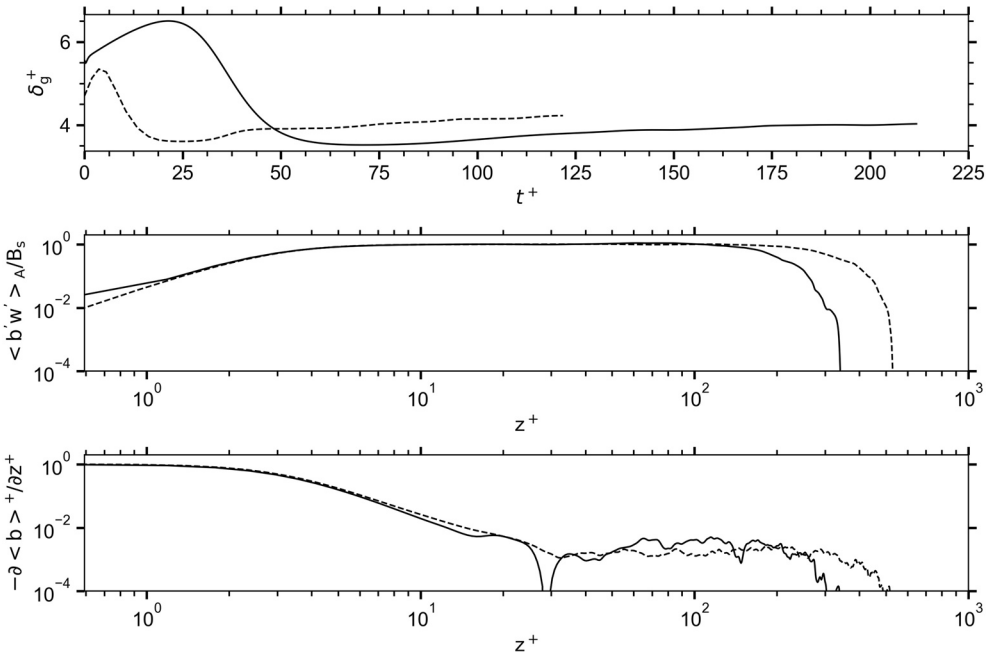

Figure A1. Comparison of simulation results from the original NsD case published in Mellado (2012) (dashed lines) with results from a similar setup simulated with the model PALM (solid lines). The following quantities are displayed (from top to bottom): the temporal evolution of the gradient thickness scaled with the diffusion length as well as the vertical profiles of the horizontally averaged turbulent and molecular contribution to the total buoyancy flux scaled with the buoyancy flux at the surface at the end of the simulation. The time is measured with respect to the time scale of the diffusion process and the height is specified in relation to the diffusion length. For more information to symbols, variables, or scaling see Mellado (2012).

The vertical profiles of the turbulent and molecular sensible heat flux also show similar shapes for both runs. The turbulent heat flux profiles overlap except close to the bottom surface and at the boundary layer top. A difference at the bottom is, in fact, only visible at the first grid point of the PALM domain. This difference is due to the higher resolution and the less dissipative advection scheme used in Mellado (2012). Both enable a better representation of the physical situation in the near-wall region. The deviations in the turbulent heat flux for 200 wall units and more are related to the different heights of the boundary layers at the end of the simulations. In both cases, the simulations are stopped when the boundary layer height is roughly 0.3 L_0. For the original high-resolution NsD case, L_0 is larger because a reference Rayleigh number of 3.6×10^9 instead of 9×10^8 was chosen (see also Equation A1). As a consequence, the boundary layer thickness at the end is higher. The different boundary layer thicknesses are also the explanation for the deviations that are visible in the profiles of the molecular heat flux for 300 wall units and more. The remaining lower part of the profiles can be approximately regarded as identical.

The final value for the gradient thickness is 4.22 in the original simulation, whereas PALM simulates a value of 4.03. This difference can be again explained by the different boundary layer thicknesses already men-

tioned above. They indicate that the turbulent flow in the original simulation is in a later state compared to the flow in the PALM simulation. Because there is a slight increase in δ_g^+ with time, it is expected that the gradient thickness of the PALM simulation would match even better if both boundary layer heights would have been the same at the end of the simulation. This is also true for the convection length scale and convective Rayleigh number defined in Mellado (2012), which show smaller values in the PALM simulation due to the shallower boundary layer.

Appendix B: Resolution Requirements

The most important requirement to perform accurate DNS is to resolve the finest length scales of the fluid. For flows with Prandtl numbers of $\mathcal{O}(1)$, the Kolmogorov length scale $\eta_K = (\nu^3 / \epsilon)^{1/4}$ (Kolmogorov, 1941) and the Obukhov-Corrsin scale $\eta_\theta = (\kappa^3 / \epsilon)^{1/4} = \eta_K Pr^{-3/4}$ (Corrsin, 1951; Obukhov, 1949) must be adequately resolved (e.g., Shishkina et al., 2010). ϵ indicates the local, instantaneous energy dissipation rate per unit mass (e.g., Hamlington et al., 2012; Pope, 2000; Shishkina et al., 2010)

$$\epsilon = \frac{\nu}{2}\left(\frac{\partial u_i'}{\partial x_j} + \frac{\partial u_j'}{\partial x_i}\right)^2, \tag{B1}$$

with u_i' the fluctuation of the velocity component u_i with respect to the horizontal mean of the velocity field. Note, the Obukhov-Corrsin scale is sometimes called the Batchelor scale (e.g., Hay & Papalexandris, 2019; Stevens et al., 2010), which is, strictly speaking, wrong. The Batchelor scale is defined as $\eta_B = (\nu\kappa^2 / \epsilon)^{1/4} = \eta_K Pr^{-1/2}$ and can be considered as the most restrictive length scale for $Pr \gg 1$ (Shishkina et al., 2010). Additionally, an accurate DNS must be able to resolve the steep velocity and temperature gradients close to the wall (Grötzbach, 1983).

The most common criterion that enables an *a priori* calculation of the allowed maximum grid width $h_{max} = \max(\Delta x, \Delta y, \Delta z)$ in the bulk of the flow is

$$h_{max} \leq \pi\eta_K = \pi\left(\frac{\nu^3}{\epsilon}\right)^{1/4}, \tag{B2}$$

$$\pi\eta_K \approx \pi H\left(\frac{Pr^2}{RaNu}\right)^{1/4}, \tag{B3}$$

$$h_{max} \leq \pi\eta_\theta = \pi\left(\frac{\kappa^3}{\epsilon}\right)^{1/4}, \tag{B4}$$

$$\pi\eta_\theta \approx \pi H\left(\frac{1}{RaPrNu}\right)^{1/4}. \tag{B5}$$

Here, Nu is the global Nusselt number, which is calculated based on the temporarily and spatially averaged turbulent heat flux (e.g., Bailon-Cuba et al., 2010; Scheel et al., 2013)

$$Nu = 1 + \frac{H}{\kappa\Delta\theta}\langle w\theta\rangle_{V,t}, \tag{B6}$$

where $\langle\cdot\rangle_{V,t}$ denotes a time and volume average over the whole model domain. The above criterion for the grid width was originally proposed by Grötzbach (1983). However, he uses the less restrictive definition of a mean grid width $(\Delta x\Delta y\Delta z)^{1/3}$, whereas Stevens et al. (2010) suggests to take the largest grid width in any spatial direction (h_{max}). When $Pr < 1$, which is true for the flows under study, equation (B2) is more restrictive and determines the maximum allowed grid spacing. To enable a calculation of h_{max}, the Nusselt number has to be known in advance. For estimating the Nusselt number, a formula derived by Scheel and Schumacher (2016) is used, which relates the Nusselt and the Rayleigh number for $Pr = 0.7$ as follows:

$$Nu = 0.15Ra^{0.29}. \tag{B7}$$

This formula allows an estimation of Nu for a given Rayleigh number and the result is used in Equation (B3) to calculate the maximum allowed grid width in the bulk of the flow before running the simulations. Regarding the setups in Table 1, Equation B3 is always fulfilled because the calculated h_{max} is larger than 3 mm for each simulation.

Additionally, the grid resolution must be evaluated *a posteriori* similar to Bailon-Cuba et al. (2010) by using Equation B2 together with the temporarily and horizontally averaged dissipation rate $\langle\epsilon(z)\rangle_t$:

$$\frac{h_{max}}{\eta_K(z)} = h_{max}\left(\frac{\nu^3}{\langle\epsilon(z)\rangle_t}\right)^{-1/4} \leq \pi. \tag{B8}$$

Figure B1 shows the above ratio over the normalized domain height for all different Rayleigh numbers and velocity boundary conditions used in this study. As expected, the profiles for no-slip boundaries peak close to the plates and are nearly constant in between, whereas the profile for the free-slip boundaries is approximately constant over the whole cell. The resolution criterion (B8) is also fulfilled for RA1010A2 and RA1010A4, which show a similar profile to simulation RA1010A3.

The criterion of Grötzbach (1983) is based on simulations with Rayleigh numbers up to 3.81×10^5 ($Pr = 0.7$) and assumes that the TKE dissipation is flat (i.e., height constant) and equals the production of TKE through buoyancy. This is especially not true in the near-wall region (Figure B1, see also Scheel & Schumacher, 2016). Thus, a different *a priori* resolution criterion must be applied to ensure that the velocity and thermal boundary layers are well-resolved. Shishkina et al. (2010) developed such a criterion based on the laminar Prandtl-Blasius boundary layer equations. It reads for $3 \times 10^{-4} \leq Pr \leq 1$:

$$h_{max} \leq 2^{-3/2} a^{-1} Nu^{-3/2} HPr^{0.5355-0.033\log(Pr)}. \tag{B9}$$

Here, a is an empirical value of 0.482. The Nusselt number can be again estimated in advance of the simulation using Equation B7. The resulting grid spacings that would guarantee a perfectly resolved DNS (according to Equation B9) are listed in Table 1. It is obvious that the cases for $Ra \geq 10^9$ insufficiently resolve the

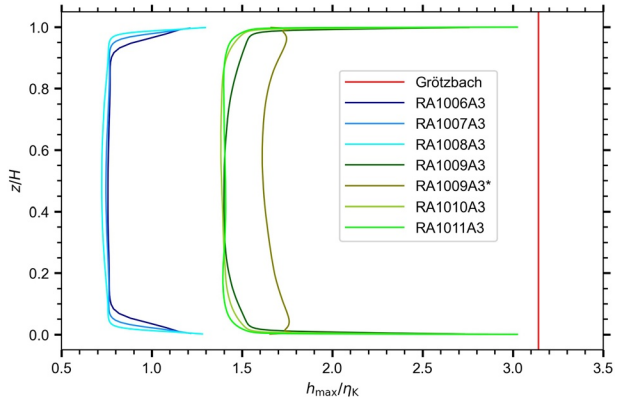

Figure B1. Ratio of the applied maximum grid width h_{max} and the Kolmogorov scale η_K for all conducted simulation with aspect ratio 3. Blue lines show the ratios for simulations with 1 mm grid spacing whereas green lines represent the ratios for simulations with 2 mm resolution. The red line indicates the limit π of the resolution criterion (B8).

boundary layers at the plates. To clarify the effect of this insufficient resolution on the dust devil statistics, a grid resolution study is performed. Results and conclusions of that study are discussed in Appendix C. Regardless of the insufficiently resolved boundary layers, the resolution criterion of Grötzbach (1983), which has been often use as the standard for evaluating the grid spacing (e.g., Bailon-Cuba et al., 2010; Shishkina & Wagner, 2007, 2008; Stevens et al., 2010), is fulfilled in all cases.

Appendix C: Grid Resolution Study

To estimate the effect of insufficiently resolved boundary layers near the plates on the dust devil statistics, three additional simulations with a Rayleigh number of 10^9, no-slip boundary conditions, an aspect ratio of $\Gamma = 3$ and grid spacings of 8, 4, and 1 mm have been conducted. Here, a grid spacing of 1 mm is regarded as a sufficient resolution according to Equation B9. In addition to these three single simulations, an ensemble of 10 members has been created for the case with 2 mm grid spacing, which is the resolution used for the main simulations introduced in Section 2.1 having a Rayleigh number larger than 10^8. With this ensemble, confidence intervals of the ensemble mean and standard deviation can be calculated with the aim to check the statistical significance of differences and similarities caused by differently resolved simulations. The focus in this section is on $Ra = 10^9$ because lower Rayleigh numbers do not show a sufficiently large number of dust devils for statistical analysis (see Section 3.3) and larger Rayleigh numbers would exceed the computational resources. The limited computing power is also the reason why an ensemble is only created for the simulation with 2 mm grid resolution. For example, the single model run with 1 mm grid spacing, 1,920 × 1,920 × 640 grid points, a simulation time of 100 s, and about 80,000 time steps consumes about 41 h CPU time on 4096 PEs of an Atos/Bull system equipped with Intel Xeon Platinum 9242 processors.

For a meaningful comparison of dust devil characteristics between differently resolved simulations, the vortex detection and analysis described in Section 2.2 has to be unified from a physical point of view. Once the dust devil centers are connected to tracks, the time period and distance, in which/where the algorithm tries to find the next dust devil center of the same track, must be the same. For all simulations, the time period is equal to three temporarily averaged model time steps of the 8 mm run (43.55 ms). Simultaneously, the maximum allowed distance to the next dust devil center of the same track must be less than or equal to 16 mm (two times the grid spacing of the 8 mm run). The physical detection height is (roughly) 4 mm in all cases, which corresponds to the first, second, third, or fifth grid point above the surface for a grid spacing of 8, 4, 2, and 1 mm, respectively.

To evaluate the convergence behavior of the dust devil statistics with decreasing grid spacing, a significance interval for the simulation with 2 mm resolution is determined as follows. At first, the 95% confidence interval of the ensemble mean μ is calculated. For example, the confidence interval for the ensemble mean of the total number of detected dust devils is [93.13, 105.87] with a central value of 99.5 (see Figure C1). Second, the 95% confidence interval of the standard deviation σ is calculated, which is [6.13, 16.27] for N. Subsequently, the upper limit of the significance interval is determined by adding the upper limit of the confidence interval of the mean (i.e., 105.87) to 2 times the upper limit of the confidence interval of the standard deviation (i.e., 32.54). For N, this results in a value of 138.41. The lower limit of the significance interval is calculated in the same way using the lower limit from [93.13, 105.87], which yields a value of 60.59. In these calculations, 2 standard deviations are considered because they cover roughly 95% of a normally distributed data set assumed here. Finally, the statistics for the simulations with 8, 4, and 1 mm grid widths are compared to the significance intervals taken from the ensemble members. If a value lies within the significance interval, the difference is considered to be statistically insignificant. In other words, it is very likely that if a value does not lie within the significance interval, the respective simulation is not part of the same ensemble and differences are statistically significant.

Figure C1 shows the averaged bulk characteristics and significance intervals of all relevant quantities for the differently resolved simulations. Here, a lifetime of 1.07 s and more is considered as long-lived because this value indicates the maximum of the lifetime frequency distribution for the 8 mm run (see also Section 2.2). N and τ are considered as almost converged for every resolution because all values are within the respective significance interval. However, for $\overline{\nu_t}$ and $\overline{r}$, a grid spacing of at least 4 mm and for $\overline{|p^*|_{max}}$, $\overline{\{u_{tan}\}_{max}}$, $\overline{\{u_{rad}\}_{max}}$, and $\overline{\{u_h\}_{max}}$, a grid spacing of at least 2 mm is necessary to adequately capture the statistics.

$\overline{|\zeta|_{max}}$ and $\overline{\{w\}_{max}}$ are not converged at all because the values for the run with 1 mm resolution (408.75 s^{-1}, 45.68 $cm\,s^{-1}$) are still far away from the upper significance interval limits (341.28 s^{-1}, 35.73 $cm\,s^{-1}$). The large deviation in the vorticity arises from the way it is calculated. In the discretized form of Equation 6, smaller grid spacings automatically create larger values because similar velocity gradients are evaluated across smaller distances. Therefore, the vorticity become larger and larger with decreasing grid width, as also the theoretical model of a line vortex suggests. To make the quantitative vorticity values in differently resolved simulations comparable, Equation 6 should have been evaluated based on the same distance, that is 8 mm. Because this did not happen by mistake, no convergence in the vorticity occurs. The vorticity eval-

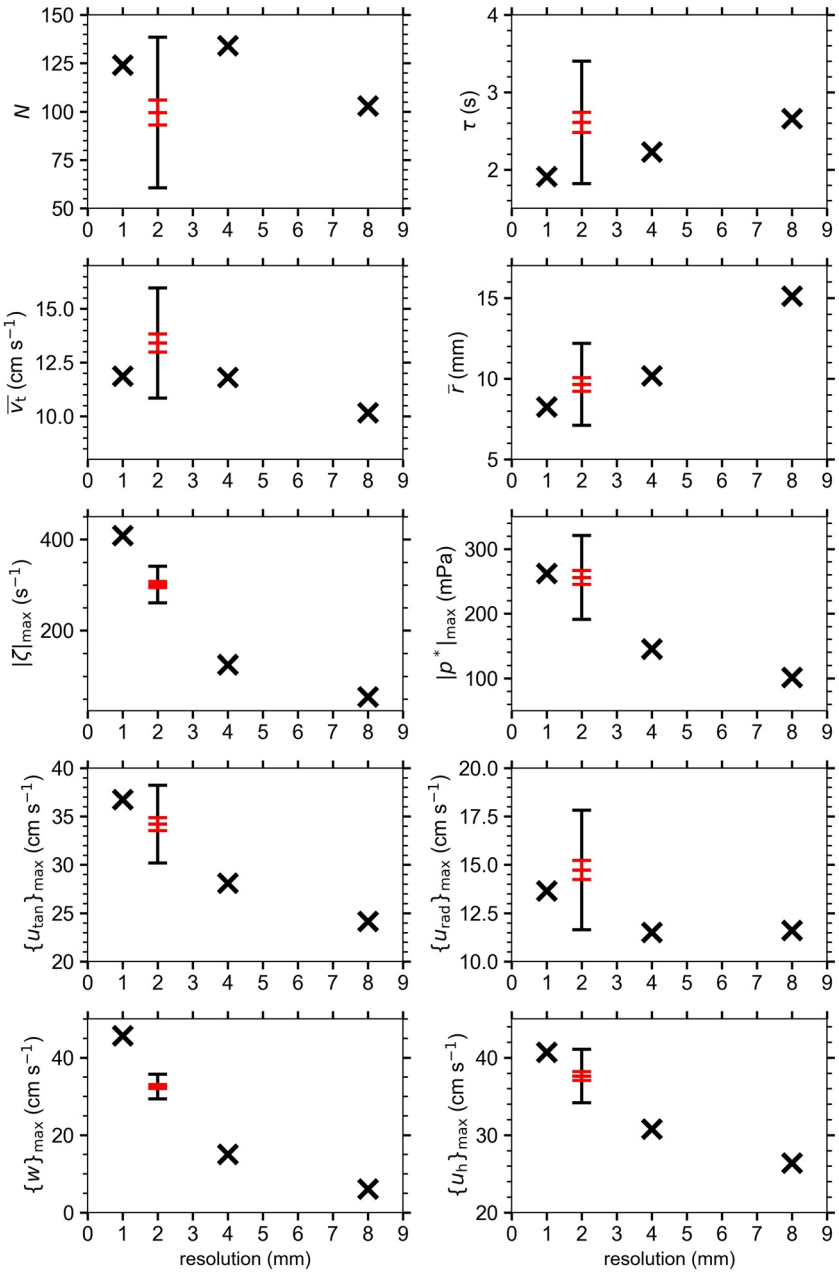

Figure C1. Dust devil characteristics for a Rayleigh number of 10^9 and an aspect ratio of 3 using a grid resolution of 8 mm, 4 mm, 2 mm, and 1 mm. Only long-lived vortices with a lifetime of more than 1.07 s are considered. Crosses mark the averaged values over all *N* dust devils. For a grid spacing of 2 mm, the 95% confidence interval of the ensemble mean with its central value (red lines) and the statistical significance interval (black lines, for explanation see text) are shown.

uated along the same distance is expected to be converged for a resolution of 2 mm because the pressure drop is already converged and vertical rotation and pressure reduction in the center are strongly connected to each other in dust devil-like vortices, as it is proposed by the theoretical model of a Rankine vortex. The reason for the large deviation in $\overline{\{w\}}_{\max}$ between all differently resolved simulations is explained through the highly localized maximum values of w that occur in the dust devil center. Our results show two pronounced regions of maximum vertical velocity (see Figure 6). These regions have extent of 10–15 mm. This spatial extent of localized vertical velocity maxima is small compared to the regions associated with tangential and radial velocity maxima. Capturing smaller regions with strong velocity fluctuations requires higher resolution. Therefore, a grid spacing of 2 mm is not fine enough to resolve the pronounced maximum values of w in the dust devils, but it is sufficient for the maximum values of tangential and radial velocity.

Limited computational resources do not allow a grid resolution study for higher Rayleigh numbers (i.e., 10^{10} and 10^{11}). With the above mentioned results for $Ra = 10^9$ and guaranteeing that the resolution criterion of Grötzbach (1983) is always fulfilled, it is assumed that a grid spacing of 2 mm is also sufficient for Rayleigh numbers up to 10^{11}, although the gap to fulfill criterion (B9) (~0.5 mm grid width for $Ra = 10^{10}$ and $Ra = 10^{11}$) is even larger compared to 1 mm for $Ra = 10^9$.

To sum up, a 2 mm grid spacing, which fulfills the resolution criterion after Grötzbach (1983), is fine enough to adequately capture most of the dust devil properties. However, quantitative comparisons of $\overline{\{w\}}_{\max}$ and $\overline{|\zeta|}_{\max}$ between simulations with different Ra, Γ, or velocity boundary conditions are avoided in this study to account for the findings mentioned in this section. But also quantitative information about the other quantities should be treated carefully because the grid resolution study has been only performed for $Ra = 10^9$. In addition, the estimates of the statistics from the main simulations (see Table 1) are based on just one ensemble member. Furthermore, single statistical values, like averaged velocities or pressure drops, are highly influenced by the detection/analysis height (see Section 2.2). A qualitative comparison of all regarded quantities is possible though without constraints.

Data Availability Statement

All simulations were performed on the Cray XC40 and Atos system of the North-German Supercomputing Alliance (HLRN-3/4) located in Berlin and Göttingen. The LES model PALM is freely available (revision 4221, http://palm.muk.uni-hannover.de/trac/browser/?rev=4221). For the validation of PALM's DNS mode, revision 3867 was used. The PALM output used to generate figures and tables is accessible via https://doi.org/10.25835/0071502. Also, the user-specific code for detecting dust devils, model steering files, and scripts for post-processing the raw data are stored there.

Acknowledgments
This work was funded by the German Research Foundation (DFG) under Grant RA 617/31-1. Open access funding enabled and organized by Projekt DEAL.

References

Bailon-Cuba, J., Emran, M. S., & Schumacher, J. (2010). Aspect ratio dependence of heat transfer and large-scale flow in turbulent convection. *Journal of Fluid Mechanics*, *655*(1), 152–173. https://doi.org/10.1017/S0022112010000820

Balme, M., & Greeley, R. (2006). Dust devils on earth and mars. *Reviews of Geophysics*, *44*(3), RG3003. https://doi.org/10.1029/2005RG000188

Bazdidi-Tehrani, F., Moghaddam, S., & Aghaamini, M. (2018). On the validity of Boussinesq approximation in variable property turbulent mixed convection channel flows. *Heat Transfer Engineering*, *39*(5), 473–491. https://doi.org/10.1080/01457632.2017.1312902

Belmonte, A., Tilgner, A., & Libchaber, A. (1994). Temperature and velocity boundary layers in turbulent convection. *Physical Review E–Statistical Physics, Plasmas, Fluids, and Related Interdisciplinary Topics*, *50*(1), 269–279. https://doi.org/10.1103/PhysRevE.50.269

Bluestein, H. B., Weiss, C. C., & Pazmany, A. L. (2004). Doppler radar observations of dust devils in Texas. *Monthly Weather Review*, *132*(1), 209–224. https://doi.org/10.1175/1520-0493(2004)132<0209:droodd>2.0.co;2

Corrsin, S. (1951). On the spectrum of isotropic temperature fluctuations in an isotropic turbulence. *Journal of Applied Physics*, *22*(4), 469–473. https://doi.org/10.1063/1.1699986

Cortese, T., & Balachandar, S. (1993). Vortical nature of thermal plumes in turbulent convection. *Physics of Fluids A: Fluid Dynamics*, *5*(12), 3226–3232. https://doi.org/10.1063/1.858679

Davies-Jones, R. (2015). A review of supercell and tornado dynamics. *Atmospheric Research*, *158–159*(1), 274–291. https://doi.org/10.1016/j.atmosres.2014.04.007

De, A. K., Eswaran, V., & Mishra, P. K. (2017). Scalings of heat transport and energy spectra of turbulent Rayleigh-Bénard convection in a large-aspect-ratio box. *International Journal of Heat and Fluid Flow*, *67*(1), 111–124. https://doi.org/10.1016/j.ijheatfluidflow.2017.08.002

Dessens, J. (1972). Influence of ground roughness on tornadoes: A laboratory simulation. *Journal of Applied Meteorology*, *11*(1), 72–75. https://doi.org/10.1175/1520-0450(1972)011<0072:iogrot>2.0.co;2

du Puits, R., Resagk, C., & Thess, A. (2013). Thermal boundary layers in turbulent Rayleigh-Bénard convection at aspect ratios between 1 and 9. *New Journal of Physics*, *15*, 013040. https://doi.org/10.1088/1367-2630/15/1/013040

du Puits, R., Resagk, C., Tilgner, A., Busse, F. H., & Thess, A. (2007). Structure of thermal boundary layers in turbulent Rayleigh-Bénard convection. *Journal of Fluid Mechanics*, *572*(1), 231–254. https://doi.org/10.1017/S0022112006003569

El Guernaoui, O., Reuder, J., Esau, I., Wolf, T., & Maronga, B. (2019). Scaling the decay of turbulence kinetic energy in the free-convective boundary layer. *Boundary-Layer Meteorology*, *173*(1), 79–97. https://doi.org/10.1007/s10546-019-00458-z

Ellehoj, M. D., Gunnlaugsson, H. P., Taylor, P. A., Kahanpää, H., Bean, K. M., Cantor, B. A., et al. (2010). Convective vortices and dust devils at the phoenix mars mission landing site. *Journal of Geophysical Research*, *115*(E4), E00E16. https://doi.org/10.1029/2009JE003413

Gheynani, B., & Kanak, K. M. (2001). Rayleigh-Bénard convection as a tool for studying dust devils. *Atmospheric Science Letters*, *2*(1), 104–113. https://doi.org/10.1006/asle.2001.0043

Gheynani, B. T., & Taylor, P. A. (2011). Large Eddy Simulation of typical dust devil-like vortices in highly convective Martian boundary layers at the Phoenix lander site. *Planetary and Space Science*, *59*(1), 43–50. https://doi.org/10.1016/j.pss.2010.10.011

Giersch, S., Brast, M., Hoffmann, F., & Raasch, S. (2019). Toward large-Eddy simulations of dust devils of observed intensity: Effects of grid spacing, background wind, and surface heterogeneities. *Journal of Geophysical Research - D: Atmospheres*, *124*(14), 7697–7718. https://doi.org/10.1029/2019JD030513

Gillette, D. A., & Sinclair, P. C. (1990). Estimation of suspension of alkaline material by dust devils in the United States. *Atmospheric Environment Part A. General Topics*, *24*(5), 1135–1142. https://doi.org/10.1016/0960-1686(90)90078-2

Gray, D. D., & Giorgini, A. (1976). The validity of the Boussinesq approximation for liquids and gases. *International Journal of Heat and Mass Transfer*, *19*(5), 545–551. https://doi.org/10.1016/0017-9310(76)90168-X

Greeley, R., Balme, M. R., Iversen, J. D., Metzger, S., Mickelson, R., Phoreman, J., & White, B. (2003). Martian dust devils: Laboratory simulations of particle threshold. *Journal of Geophysical Research*, *108*(E5), 5041. https://doi.org/10.1029/2002JE001987

Grossmann, S., & Lohse, D. (2002). Prandtl and Rayleigh number dependence of the Reynolds number in turbulent thermal convection. *Physical Review E - Statistical Physics, Plasmas, Fluids, and Related Interdisciplinary Topics*, *66*(1), 016305. https://doi.org/10.1103/PhysRevE.66.016305

Grötzbach, G. (1983). Spatial resolution requirements for direct numerical simulation of the Rayleigh-Bénard convection. *Journal of Computational Physics*, *49*(2), 241–264. https://doi.org/10.1016/0021-9991(83)90125-0

Gu, Z., Wei, W., & Zhao, Y. (2010). An overview of surface conditions in numerical simulations of dust devils and the consequent near-surface air flow fields. *Aerosol Air Quality Research*, *10*(3), 272–281. https://doi.org/10.4209/aaqr.2009.12.0077

Hamlington, P. E., Krasnov, D., Boeck, T., & Schumacher, J. (2012). Local dissipation scales and energy dissipation-rate moments in channel flow. *Journal of Fluid Mechanics*, *701*(1), 419–429. https://doi.org/10.1017/jfm.2012.170

Han, Y., Wang, K., Liu, F., Zhao, T., Yin, Y., Duan, J., & Luan, Z. (2016). The contribution of dust devils and dusty plumes to the aerosol budget in western China. *Atmospheric Environment*, *126*, 21–27. https://doi.org/10.1016/j.atmosenv.2015.11.025

Hay, W. A., & Papalexandris, M. V. (2019). Numerical simulations of turbulent thermal convection with a free-slip upper boundary. *Proceedings of the Royal Society A*, *475*(2232), 20190601. https://doi.org/10.1098/rspa.2019.0601

Heinze, R., Raasch, S., & Etling, D. (2012). The structure of Kármán vortex streets in the atmospheric boundary layer derived from large eddy simulation. *Metz*, *21*(3), 221–237. https://doi.org/10.1127/0941-2948/2012/0313

Iijima, R., & Tamura, T. (2008). *DNS on growth of a vertical vortex in convection due to external forces*. In Paper presented at 24th Conference on Severe Local Storms. Savannah: American Meteorological Society.

Ito, J., & Niino, H. (2013). Formation mechanism of dust devil-like vortices in idealized convective mixed layers. *Journal of the Atmospheric Sciences*, *70*(4), 1173–1186. https://doi.org/10.1175/JAS-D-12-085.1

Ito, J., Niino, H., & Nakanishi, M. (2010). Large Eddy simulation on dust suspension in a convective mixed layer. *Solanus*, *6*(1), 133–136. https://doi.org/10.2151/sola.2010-034

Jemmett-Smith, B. C., Marsham, J. H., Knippertz, P., & Gilkeson, C. A. (2015). Quantifying global dust devil occurrence from meteorological analyses. *Geophysical Research Letters*, *42*(4), 1275–1282. https://doi.org/10.1002/2015GL063078

Kahanpää, H., Newman, C., Moores, J., Zorzano, M.-P., Martín-Torres, J., Navarro, S., et al. (2016). Convective vortices and dust devils at the MSL landing site: Annual variability. *Journal of Geophysical Research: Planets*, *121*(8), 1514–1549. https://doi.org/10.1002/2016JE005027

Kanak, K. M. (2005). Numerical simulation of dust devil-scale vortices. *Quarterly Journal of the Royal Meteorological Society*, *131*(607), 1271–1292. https://doi.org/10.1256/qj.03.172

Kanak, K. M. (2006). On the numerical simulation of dust devil-like vortices in terrestrial and Martian convective boundary layers. *Geophysical Research Letters*, *33*(19), L19S05. https://doi.org/10.1029/2006GL026207

Kanak, K. M., Lilly, D. K., & Snow, J. T. (2000). The formation of vertical vortices in the convective boundary layer. *Quarterly Journal of the Royal Meteorological Society*, *126*(569), 2789–2810. https://doi.org/10.1002/qj.49712656910

Koch, J., & Renno, N. O. (2005). The role of convective plumes and vortices on the global aerosol budget. *Geophysical Research Letters*, *32*(18), L18806. https://doi.org/10.1029/2005GL023420

Kolmogorov, A. N. (1941). The local structure of turbulence in incompressible viscous fluid for very large Reynolds numbers. *Doklady Akademiia Nauk SSSR*, *30*(1), 301–305.

Kurgansky, M. V., Lorenz, R. D., Renno, N. O., Takemi, T., Gu, Z., & Wei, W. (2016). Dust devil steady-state structure from a fluid dynamics perspective. *Space Science Reviews*, *203*(1–4), 209–244. https://doi.org/10.1007/s11214-016-0281-0

Loesch, A., & du Puits, R. (2020). *Investigation of dust devil-like vortices in a large-scale laboratory experiment using particle tracking velocimetry*. In Paper presented at EGU General Assembly 2020 (Online). European Geosciences Union.

Lorenz, R. (2011). On the statistical distribution of dust devil diameters. *Icarus*, *215*(1), 381–390. https://doi.org/10.1016/j.icarus.2011.06.005

Lorenz, R. D., & Jackson, B. K. (2016). Dust devil populations and statistics. *Space Science Reviews*, *203*(1), 277–297. https://doi.org/10.1007/s11214-016-0277-9

Lorenz, R. D., & Myers, M. J. (2005). Dust devil hazard to avition a review of united states air accident reports. *Journal of Meteorology*, *30*(298), 178–184.

Maronga, B., Banzhaf, S., Burmeister, C., Esch, T., Forkel, R., Fröhlich, D., et al. (2020). Overview of the PALM model system 6.0. *Geoscientific Model Development*, *13*(3), 1335–1372. https://doi.org/10.5194/gmd-13-1335-2020

Maronga, B., Gryschka, M., Heinze, R., Hoffmann, F., Kanani-Sühring, F., Keck, M., et al. (2015). The parallelized large-eddy simulation model (PALM) version 4.0 for atmospheric and oceanic flows: Model formulation, recent developments, and future perspectives. *Geoscientific Model Development*, *8*(8), 2515–2551. https://doi.org/10.5194/gmd-8-2515-2015

Maronga, B., & Raasch, S. (2013). Large-eddy simulations of surface heterogeneity effects on the convective boundary layer during the LITFASS-2003 experiment. *Boundary-Layer Meteorology*, *146*(1), 17–44. https://doi.org/10.1007/s10546-012-9748-z

Mellado, J. P. (2012). Direct numerical simulation of free convection over a heated plate. *Journal of Fluid Mechanics*, *712*(1), 418–450. https://doi.org/10.1017/jfm.2012.428

Morton, B. R. (1966). Geophysical vortices. *Progress in Aerospace Sciences*, *7*(1), 145–194. https://doi.org/10.1016/0376-0421(66)90008-X
Murphy, J., Steakley, K., Balme, M., Deprez, G., Esposito, F., Kahanpää, H., et al. (2016). Field measurements of terrestrial and Martian dust devils. *Space Science Reviews*, *203*(1), 39–87. https://doi.org/10.1007/s11214-016-0283-y
Neakrase, L. D. V., & Greeley, R. (2010). Dust devils in the laboratory: Effect of surface roughness on vortex dynamics. *Journal of Geophysical Research*, *115*(E5), E05003. https://doi.org/10.1029/2009JE003465
Niemela, J. J., & Sreenivasan, K. R. (2003). Confined turbulent convection. *Journal of Fluid Mechanics*, *481*(1), 355–384. https://doi.org/10.1017/S0022112003004087
Nishizawa, S., Odaka, M., Takahashi, Y. O., Sugiyama, K.-i., Nakajima, K., Ishiwatari, M., et al. (2016). Martian dust devil statistics from high-resolution large-eddy simulations. *Geophysical Research Letters*, *43*(9), 4180–4188. https://doi.org/10.1002/2016GL068896
Obukhov, A. M. (1949). Structure of the temperature field in turbulent streams. *Izvestija Akademii Nauk SSSR Seriya Geograficheskaya I Geofizicheskaya*, *13*(1), 58–69.
Ohno, H., & Takemi, T. (2010). Mechanisms for intensification and maintenance of numerically simulated dust devils. *Atmospheric Science Letters*, *11*(1). https://doi.org/10.1002/asl.249
Pandey, A., Scheel, J. D., & Schumacher, J. (2018). Turbulent superstructures in Rayleigh-Bénard convection. *Nature Communications*, *9*(1), 2118. https://doi.org/10.1038/s41467-018-04478-0
Parodi, A., von Hardenberg, J., Passoni, G., Provenzale, A., & Spiegel, E. A. (2004). Clustering of plumes in turbulent convection. *Physical Review Letters*, *92*(19), 194503. https://doi.org/10.1103/PhysRevLett.92.194503
Patrinos, A. A. N., & Kistler, A. L. (1977). A numerical study of the Chicago lake breeze. *Boundary-Layer Meteorology*, *12*(1), 93–123. https://doi.org/10.1007/BF00116400
Pope, S. B. (2000). *Turbulent flows*. Cambridge: Cambridge University Press. https://doi.org/10.1017/CBO9780511840531
Raasch, S., & Franke, T. (2011). Structure and formation of dust devil-like vortices in the atmospheric boundary layer: A high-resolution numerical study. *Journal of Geophysical Research*, *116*(D16), D16120. https://doi.org/10.1029/2011JD016010
Rafkin, S., Haberle, R. M., & Michaels, T. I. (2001). The Mars regional atmospheric modeling system: Model description and selected simulations. *Icarus*, *151*(2), 228–256. https://doi.org/10.1006/icar.2001.6605
Rafkin, S., Jemmett-Smith, B., Fenton, L., Lorenz, R., Takemi, T., Ito, J., & Tyler, D. (2016). Dust devil formation. *Space Science Reviews*, *203*(1), 183–207. https://doi.org/10.1007/s11214-016-0307-7
Renno, N. O., Abreu, V. J., & Koch, J. (2004). Matador 2002: A pilot field experiment on convective plumes and dust devils. *Journal of Geophysical Research*, *109*(E7), E07001. https://doi.org/10.1029/2003JE002219
Rizza, U., Miglietta, M. M., Degrazia, G. A., Acevedo, O. C., & Marques Filho, E. P. (2013). Sunset decay of the convective turbulence with large-eddy simulation under realistic conditions. *Physica A: Statistical Mechanics and Its Applications*, *392*(19), 4481–4490. https://doi.org/10.1016/j.physa.2013.05.009
Roberts, B., & Xue, M. (2017). The role of surface drag in mesocyclone intensification leading to tornadogenesis within an idealized supercell simulation. *Journal of the Atmospheric Sciences*, *74*(9), 3055–3077. https://doi.org/10.1175/JAS-D-16-0364.1
Roberts, B., Xue, M., Schenkman, A. D., & Dawson, D. T. (2016). The role of surface drag in tornadogenesis within an idealized supercell simulation. *Journal of the Atmospheric Sciences*, *73*(9), 3371–3395. https://doi.org/10.1175/JAS-D-15-0332.1
Rotunno, R. (2013). The fluid dynamics of tornadoes. *Annual Review of Fluid Mechanics*, *45*(1), 59–84. https://doi.org/10.1146/annurev-fluid-011212-140639
Ryan, J. A. (1972). Relation of dust devil frequency and diameter to atmospheric temperature. *Journal of Geophysical Research*, *77*(36), 7133–7137. https://doi.org/10.1029/JC077i036p07133
Sakievich, P. J., Peet, Y. T., & Adrian, R. J. (2016). Large-scale thermal motions of turbulent Rayleigh-Bénard convection in a wide aspect-ratio cylindrical domain. *International Journal of Heat and Fluid Flow*, *61*(1), 183–196. https://doi.org/10.1016/j.ijheatfluidflow.2016.04.011
Scheel, J. D., Emran, M. S., & Schumacher, J. (2013). Resolving the fine-scale structure in turbulent Rayleigh-Bénard convection. *New Journal of Physics*, *15*(11), 113063. https://doi.org/10.1088/1367-2630/15/11/113063
Scheel, J. D., & Schumacher, J. (2014). Local boundary layer scales in turbulent Rayleigh-Bénard convection. *Journal of Fluid Mechanics*, *758*(1), 344–373. https://doi.org/10.1017/jfm.2014.536
Scheel, J. D., & Schumacher, J. (2016). Global and local statistics in turbulent convection at low Prandtl numbers. *Journal of Fluid Mechanics*, *802*(1), 147–173. https://doi.org/10.1017/jfm.2016.457
Shao, Y., Wyrwoll, K.-H., Chappell, A., Huang, J., Lin, Z., McTainsh, G. H., et al. (2011). Dust cycle: An emerging core theme in earth system science. *Aeolian Research*, *2*(4), 181–204. https://doi.org/10.1016/j.aeolia.2011.02.001
Shi, N., Emran, M. S., & Schumacher, J. (2012). Boundary layer structure in turbulent Rayleigh-Bénard convection. *Journal of Fluid Mechanics*, *706*(1), 5–33. https://doi.org/10.1017/jfm.2012.207
Shishkina, O., Stevens, R. J. A. M., Grossmann, S., & Lohse, D. (2010). Boundary layer structure in turbulent thermal convection and its consequences for the required numerical resolution. *New Journal of Physics*, *12*(7), 075022. https://doi.org/10.1088/1367-2630/12/7/075022
Shishkina, O., & Wagner, C. (2007). Local heat fluxes in turbulent Rayleigh-Bénard convection. *Physics of Fluids*, *19*(8), 085107. https://doi.org/10.1063/1.2756583
Shishkina, O., & Wagner, C. (2008). Analysis of sheet-like thermal plumes in turbulent Rayleigh-Bénard convection. *Journal of Fluid Mechanics*, *599*(1), 383–404. https://doi.org/10.1017/S002211200800013X
Sinclair, P. C. (1969). General characteristics of dust devils. *Journal of Applied Meteorology*, *8*(1), 32–45. https://doi.org/10.1175/1520-0450(1969)008⟨0032:GCODD⟩2.0.CO;2
Sinclair, P. C. (1973). The lower structure of dust devils. *Journal of the Atmospheric Sciences*, *30*(8), 1599–1619. https://doi.org/10.1175/1520-0469(1973)030⟨1599:TLSODD⟩2.0.CO;
Sorbjan, Z. (1996). Joint effects of subgrid-scale diffusion and truncation errors in large-eddy simulations of the convective boundary layer. *Boundary-Layer Meteorology*, *79*(1), 181–189. https://doi.org/10.1007/BF00120080
Spiga, A., Barth, E., Gu, Z., Hoffmann, F., Ito, J., Jemmett-Smith, B., et al. (2016). Large-eddy simulations of dust devils and convective vortices. *Space Science Reviews*, *203*(1), 245–275. https://doi.org/10.1007/s11214-016-0284-x
Stevens, R. J. A. M., Blass, A., Zhu, X., Verzicco, R., & Lohse, D. (2018). Turbulent thermal superstructures in Rayleigh-Bénard convection. *Physical Review Fluids*, *3*(4), 041501. https://doi.org/10.1103/PhysRevFluids.3.041501
Stevens, R. J. A. M., Verzicco, R., & Lohse, D. (2010). Radial boundary layer structure and Nusselt number in Rayleigh-Bénard convection. *Journal of Fluid Mechanics*, *643*(1), 495–507. https://doi.org/10.1017/S0022112009992461
Sullivan, P. P., McWilliams, J. C., & Moeng, C.-H. (1994). A subgrid-scale model for large-eddy simulation of planetary boundary-layer flows. *Boundary-Layer Meteorology*, *71*(3), 247–276. https://doi.org/10.1007/BF00713741

Toigo, A. D., Richardson, M. I., Ewald, S. P., & Gierasch, P. J. (2003). Numerical simulation of Martian dust devils. *Journal of Geophysical Research*, *108*(E6), 5047. https://doi.org/10.1029/2002JE002002

van der Poel, E. P., Stevens, R. J. A. M., Sugiyama, K., & Lohse, D. (2012). Flow states in two-dimensional Rayleigh-Bénard convection as a function of aspect-ratio and Rayleigh number. *Physics of Fluids*, *24*(8), 085104. https://doi.org/10.1063/1.4744988

van Reeuwijk, M., Jonker, H. J. J., & Hanjalić, K. (2008). Wind and boundary layers in Rayleigh-Bénard convection. I. Analysis and modeling. *Physical Review E - Statistical Physics, Plasmas, Fluids, and Related Interdisciplinary Topics*, *77*(3), 036311. https://doi.org/10.1103/PhysRevE.77.036311

von Hardenberg, J., Parodi, A., Passoni, G., Provenzale, A., & Spiegel, E. A. (2008). Large-scale patterns in Rayleigh-Bénard convection. *Physics Letters A*, *372*(13), 2223–2229. https://doi.org/10.1016/j.physleta.2007.10.099

Wicker, L. J., & Skamarock, W. C. (2002). Time-splitting methods for elastic models using forward time schemes. *Monthly Weather Review*, *130*(8), 2088–2097. https://doi.org/10.1175/1520-0493(2002)130%E82088:TSMFEM%E92.0.CO;2

Wilkins, E. M., Sasaki, Y., & Johnson, H. L. (1975). Surface friction effects on thermal convection in a rotating fluid: A laboratory simulation. *Monthly Weather Review*, *103*(4), 305–317. https://doi.org/10.1175/1520-0493(1975)103⟨0305:SFEOTC⟩2.0.CO;2

Williamson, J. H. (1980). Low-storage runge-kutta schemes. *Journal of Computational Physics*, *35*(1), 48–56. https://doi.org/10.1016/0021-9991(80)90033-9

Wyngaard, J. C. (2010). *Turbulence in the atmosphere*. Cambridge: Cambridge University Press. https://doi.org/10.1017/CBO9780511840524

Zhao, Y. Z., Gu, Z. L., Yu, Y. Z., Ge, Y., Li, Y., & Feng, X. (2004). Mechanism and large eddy simulation of dust devils. *Atmosphere-Ocean*, *42*(1), 61–84. https://doi.org/10.3137/ao.420105

Zou, H.-Y., Zhou, W-F., Chen, X., Bao, Y., Chen, J., She, Z.-S., & She, Z.-S. (2019). Boundary layer structure in turbulent Rayleigh-Bénard convection in a slim box. *Acta Mechanica Sinica*, *35*(4), 713–728. https://doi.org/10.1007/s10409-019-00874-x